Design and Characterization of a Dumbbell Micro-Ring Resonator Reflector

by

Han Yun

B.A.Sc., The University of British Columbia, 2009

A THESIS SUBMITTED IN PARTIAL FULFILLMENT OF
THE REQUIREMENTS FOR THE DEGREE OF

MASTER OF APPLIED SCIENCE

in

The Faculty of Graduate Studies

(Electrical and Computer Engineering)

THE UNIVERSITY OF BRITISH COLUMBIA

(Vancouver)

May 2013

Abstract

A dumbbell shape micro-ring resonator reflector fabricated using the silicon-on-insulator (SOI) technology for use as a reflective notch filter is presented. The development of this dumbbell micro-ring reflector is motivated by the increasing demand for highly confined resonant structures as integrated optical components in modern optical communication and sensor applications. In this thesis, we have analyzed and simulated the reflection properties of dumbbell micro-ring reflectors based on SOI strip waveguides. We have optimized our design based on the analytic modeling and simulation results and had our devices fabricated at a foundry. An automated optical probe station has been developed for characterizing the performance of the fabricated dumbbell micro-ring reflectors. Measurement results on the reflection spectrum showed an extinction ratio of 20 dB with a quality factor of ∼11,000. Thermal tuning responses showed the potential for those resonators in sensor applications.

Preface

I am the main author of the conference publications titled, "Design of a Microring Reflector with a Dumbbell Structure"[29] and "Dumbbell Micro-Ring Reflector"[30]. I proposed the design of the dumbbell micro-ring reflector, modeled and simulated the device using analytic and numerical methods, and optimized its performance for fabrication. I then created a design mask layout that was fabricated by Imec in Belgium. I characterized the device using an automated measurement system, implemented and developed by Charlie Lin and me. Dr. Nicolas Jaeger, my supervisor, and Dr. Lukas Chrostowski guided my research by providing important insights into the design of the device as well as editing drafts of the conference paper and poster.

I am one of the co-authors in numerous conference and journal papers. Collaborating with other colleagues, I have been involved in many research projects during my Master's studies. In these projects, I participated in various photonic device designs including waveguide Bragg grating filters, micro-disk reflectors, grating-assisted micro-ring filters, contra-directional couplers, vernier racetrack resonators, CWDM demultiplexers, and adiabatic 3-dB couplers.

The list of publications as main author includes:

1. H. Yun, W. Shi, Y. Wang, L.Chrostowski, and N. A. F. Jaeger, "2x2

Adiabatic 3-dB Coupler on Silicon-on-Insulator Rib Waveguides", Photonics North 2013, Ottawa, Canada, accepted.

2. H. Yun, W. Shi, X. Wang, L. Chrostowski, and N. A. F. Jaeger, "Dumbbell Micro-Ring Reflector", Proc. SPIE, Photonics North 2012, vol. 8412, pp. 84120P, 10/2012.

3. H. Yun, W. Shi, X. Wang, L. Chrostowski, and N. A. F. Jaeger, "Design of a Microring Reflector with a Dumbbell Structure", The 15th Canadian Semiconductor Science and Technology Conference, 06/2011.

The list of publications as co-authors include:

1. X. Wang, H. Yun, and L. Chrostowski, "Integrated Bragg Gratings in Spiral Waveguides", CLEO (Conference on Lasers and Electro-Optics): 2013, San Jose, US, accepted.

2. W. Shi, H. Yun, C. Lin, X. Wang, J. Flueckiger, N. A. F. Jaeger, and L. Chrostowski, "Silicon CWDM Demultiplexers Using Contra-Directional Couplers", CLEO (Conference on Lasers and Electro-Optics): 2013, San Jose, US, accepted.

3. W. Shi, H. Yun, C. Lin, M. Greenberg, X. Wang, Y. Wang, S. T. Fard, J. Flueckiger, N. A. F. Jaeger, and L. Chrostowski, "Ultra-compact, at-top demultiplexer using anti-reection contra-directional couplers for CWDM networks on silicon", Opt. Express, Vol. 21, No. 6, pp. 6733-6738, 03/2013.

4. R. Boeck, J. Flueckiger, H. Yun, L. Chrostowski, N. A. F. Jaeger, "High Performance Vernier Racetrack Resonators", Opt. Letters, Vol. 37, No. 24, pp. 5199-5201, 12/2012

5. W. Shi, X. Wang, C. Lin, H. Yun, Y. Liu, T. Baehr-Jones, M. Hochberg, N. A. F. Jaeger, L. Chrostowski,, "Electrically tunable resonant

filters in phase-shifted contra-directional couplers", IEEE Group IV Photonics Conference, pp. 78-80, 09/2012

6. W. Shi, H. Yun, W. Zhang, C. Lin, T. K. Chang, Y. Wang, N. A. F. Jaeger, and L. Chrostowski, "Ultra-compact, high-Q silicon microdisk reflectors", Opt. Express, Vol. 20, Issue 20, pp. 21840-21846, 09/2012.

7. X. Wang, W. Shi, H. Yun, S. Grist, N. A. F. Jaeger, and L. Chrostowski, "Narrow-band waveguide Bragg gratings on SOI wafers with CMOS-compatible fabrication process", Opt. Express, Vol. 20, Issue 14, pp. 15547-15558, 07/2012.

8. W. Shi, T. K. Chang, H. Yun, W. Zhang, C. Lin, N. A. F. Jaeger, and L. Chrostowski, "Differential measurement of transmission losses of integrated optical components using waveguide ring resonators", Photonics North, Montreal, Canada, 06/2012.

9. W. Shi, X. Wang, W. Zhang, H. Yun, N. A. F. Jaeger, and L. Chrostowski, "Integrated microring add-drop filters with contradirectional couplers ", CLEO (Conference on Lasers and Electro-Optics) 2012, San Jose, US, pp. JW4A.91 , 05/2012.

10. W. Shi, X. Wang, H. Yun, W. Zhang, N. A. F. Jaeger, and L. Chrostowski, "Integrated silicon contradirectional couplers: modeling and experiment", SPIE Photonics Europe, Brussels, Belgium, pp. 8424-82, 04/2012.

11. W. Shi, X. Wang, H. Yun, W. Zhang, L. Chrostowski, and N. A. F. Jaeger, "Add-drop filters in silicon grating-assisted asymmetric couplers ", OFC/NFOEC, Los Angeles, US, pp. OTh3D.3 , 04/2012.

12. W. Shi, X. Wang, W. Zhang, H. Yun, C. Lin, L. Chrostowski, and N. A. F. Jaeger, "Grating-coupled silicon microring resonators", Applied

Physics Letters, Vol. 100, Issue 12, pp. 121118 - 121118-4, 03/2012.

13. L. Chrostowski, S. Grist, J. Flueckiger, W. Shi, X. Wang, E. Ouellet, H. Yun, M. Webb, B. Nie, Z. Liang, K. C. Cheung, S. A. Schmidt, D. M. Ratner, and N. A. F. Jaeger, "Silicon photonic resonator sensors and devices", Proceedings of SPIE Volume 8236; Laser Resonators, Microresonators, and Beam Control XIV, 01/2012.

14. X. Wang, W. Shi, S. Grist, H. Yun, N. A. F. Jaeger, and L. Chrostowski, "Narrow-Band Transmission Filter using Phase-Shifted Bragg Gratings in SOI Waveguide", IEEE Photonics Conference, pp. ThZ1, 10/2011.

Table of Contents

List of Tables

List of Figures

Acknowledgements

I would like to thank my parents and fiancée for their continuous support, encouragement, and faith throughout my education.

I would like to express my gratitude to my supervisor, Dr. Nicolas A. F. Jaeger, for suggesting this project, and to Drs. Nicolas A.F. Jaeger and Lukas Chrostowski for providing continual guidance and support during my research.

My thanks extend to those individuals in the Electrical and Computer Engineering Department who have helped me during my research, specially Dr. Wei Shi, Xu Wang, Charlie Lin, Miguel Ángel Guillén Torres, Jonas Flueckiger, and Dr. Mark Greenberg.

I gratefully acknowledge the support of the Natural Sciences and Engineering Research Council (NSERC) of Canada.

Furthermore, I would also like to acknowledge CMC Microsystems for the provision of services that facilitated this research, Lumerical Solutions, Inc. and Design Workshop Technologies for the design tools.

Dedication

To my father, Qinglong Yun, my mother, Gexin Jin, and my fiancée, Xiaoran Ma, whose unconditional love, continuous support, encouragement, and faith have given me the strength to overcome obstacles and to succeed in so many aspects and areas of my life.

Chapter 1

Introduction

1.1 Silicon Photonics in Optical Communications and Optical Interconnects

The implementation of photonic integrated circuits demonstrates the convergence of technological sophistication and economics of scale made possible by using silicon substrates. More specifically, in them, silicon is used as an optical waveguide medium as well as an active medium[9, 10]. The low cost of high crystal quality silicon wafers, and its high compatibility with mature silicon IC manufacturing techniques, have greatly promoted the rapid growth of silicon photonics in recent years. The strong optical confinement, offered by the high refractive index contrast between silicon and silicon dioxide, scales down the feature size of photonic circuits, which are implemented on the silicon-on-insulator (SOI) platform, to the sub-micrometer level and thus provides for highly compact photonic circuits and devices [9, 10]. Fabricated using CMOS (Complementary Metal-Oxide-Semiconductor) compatible processes, silicon photonic circuits have the potential to be integrated with CMOS VLSI (Very Large Scale Integration) chips, for added electronic-photonic functionality.

The potential for integrating silicon photonic circuits with CMOS VLSI microelectronic chips has drawn great interest from some of the world's leading companies, such as IBM and Intel, who see silicon photonics as a means to satisfy the increasing demands for ultra-fast data transfer between and within microchips, while being able to be fabricated using established CMOS facilities[12, 15]. In 2012, for the first time, IBM demonstrated single-die multichannel wavelength-mulitplexed 25Gbps transceivers by integrating optical silicon modulators and germanium photodetectors into NMOS (n-type metal-oxide-semiconductor) circuitry using standard 90nm semiconductor fabrication processes[2]. This technology breakthrough illustrates the advantages of integrating silicon photonics with electronics and offers great potential for delivering ultra-high rates data in optical interconnect applications.

Furthermore, silicon is well suited for the fabrication of photonic devices. Many applications have been demonstrated in the 1.3 - 1.6 μm wavelength range including discrete optical components, such as splitters, directional couplers, and ring resonators. Also, optical systems based on these components, such as wavelength-division multiplexing (WDM) systems, have been demonstrated within that wavelength range.

1.2 Thesis Objective

The excellent performance given by highly confined resonant structures has drawn great interest for integrated optical components in modern optical communication systems[1]. Micro-ring reflectors (MRRs), with the advantages of easy fabrication and monolithic integration with other photonic devices, can serve as alternative components for distributed Bragg reflectors (DBRs) in applications such as, reflective filters, sensors, and optical switches[6, 13, 17]. Under special circumstances, MRRs, as reflective filters, have the advantage in applications in which a single input/output fibre is preferred[17, 20]. Functioning as wavelength-selective reflectors, MRRs can be fabricated using SOI technology and be integrated into photonic integrated circuits.

The concept of wavelength-selective reflectors using micro-ring resonators was first proposed by Poon et al. in 2004[13]. They investigated the reflection properties of a circular array of coupled micro-ring resonators and showed that a micro-ring array consisting of an odd number (N$\geq$3) of rings, and with one ring coupled to the input/output (I/O) waveguide exhibited narrow bandwidth reflection, whereas an array consisting of an even number (N$\geq$4) of rings had no reflection (see Fig. 1.1a). Poon et al. simulated the micro-ring structures with radii of 125 μm. Chremmos et al.[4] and Chung et al.[6] analyzed and discussed the double-ring/coupled-ring reflector using two parallel-coupled circular micro-rings. In their papers, two parallel-coupled micro-rings were both coupled to the I/O waveguide and showed narrow bandwidth reflective behavior (see Fig. 1.1b). Chung et al.

demonstrated an MRR with two rings with radii of 50 μm. Shi et al.[17], in 2009, demonstrated an MRR using a micro-ring resonator integrated with a waveguide crossing structure, with low-loss and low-crosstalk, but which required a double-etch scheme in the fabrication (see Fig. 1.1c).

Here, we present a "dumbbell" shape micro-ring resonator reflector which has a dumbbell shape racetrack micro-ring structure coupled to a strip waveguide to achieve reflection (see Fig. 1.1d). Our device, without the need for additional complex lithography and processing steps, but with a small foot-print containing rings with radii of 30 μm, shows high reflectivity and high extinction ratio, and has the potential to be used as a wavelength-selective notch filter in optical communication systems or as various types of sensors in sensing systems.

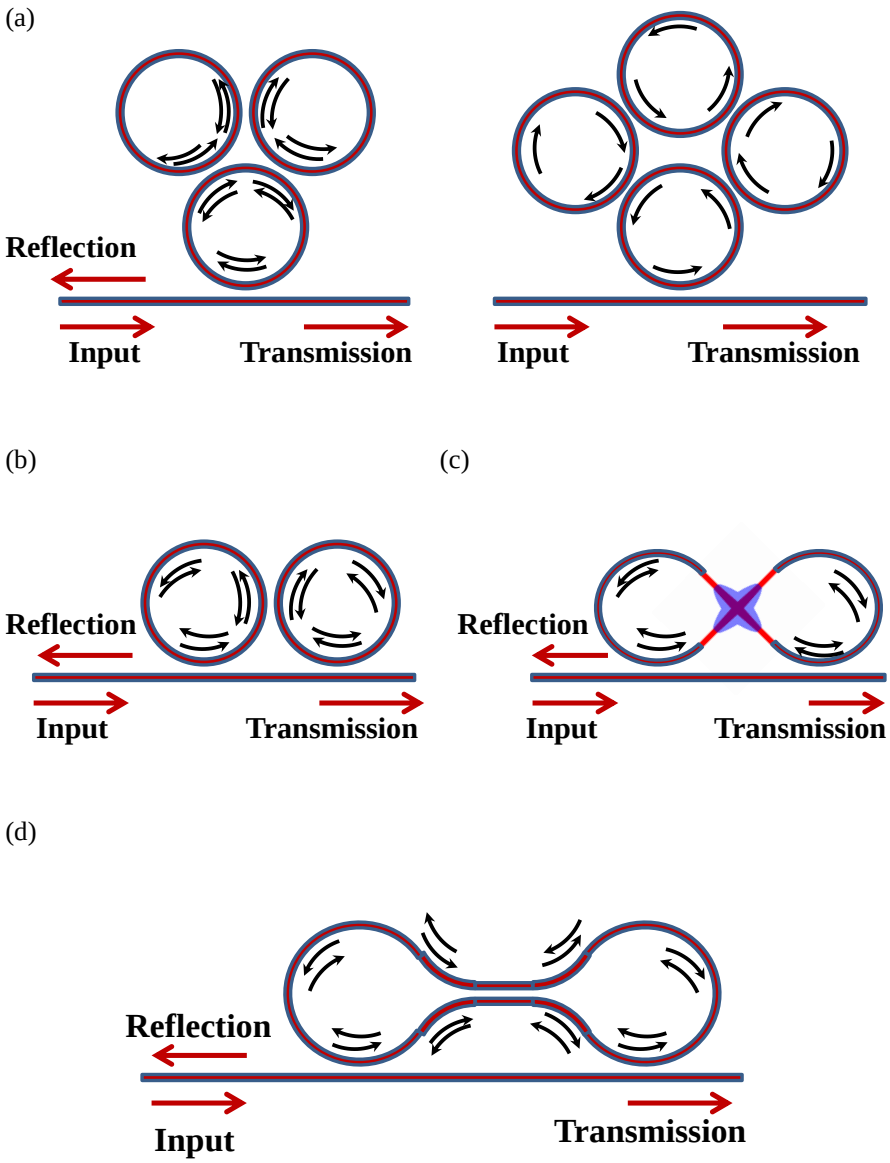

Figure 1.1: Schematics of micro-ring reflectors: (a) circular array of coupled micro-rings; (b) parallel-coupled micro-ring reflector; (c) micro-ring reflector with a waveguide cross; (b) dumbbell micro-ring reflector.

1.3 Thesis Organization

This thesis consists of five chapters. In Chapter 1, we introduce and review the development of silicon photonics in modern optical communication systems and optical interconnect applications. The motivation of this thesis is also presented. In Chapter 2, we show the background theory as well as the analytic modeling of directional couplers. Single ring resonator add-drop filters and dumbbell micro-ring resonator reflectors are analyzed using the transfer-matrix method. Also, simulation results of the reflection properties of the dumbbell micro-ring reflectors are presented in this chapter. In Chapter 3, the automated measurement system developed for characterizing on-chip silicon photonic circuits is described, and its performance is shown. In Chapter 4, the implementation of dumbbell micro-ring reflectors is provided. Experimental results of an optimized dumbbell micro-ring notch reflector are presented. Lastly, in Chapter 5, conclusion and some suggestions for future research are given.

Chapter 2

Design, Analysis, and Simulation

In this chapter, we present the design, analysis, and simulation of dumbbell micro-ring reflectors. We describe the mechanisms that result in the reflection properties of the device. Since waveguide directional couplers are important components in our device, we use a transfer-matrix method derived from supermode theory to analyze the light transfer between the two parallel coupled waveguides comprising the directional couplers. We show the derivation of the transfer functions of single ring resonator add-drop filters in forms of 2x2 matrices using the transfer-matrix method. We expand the transfer matrices, and apply the transfer-matrix method to obtain an analytic model for dumbbell micro-ring reflectors. We then calculate the reflectivities of the dumbbell micro-ring reflector and do numerical simulations in MATLAB to characterize the reflection properties of the device.

2.1 Design Approach

Our device, which contains three directional couplers, has the shape of a dumbbell (see Fig. 2.1). The reflector consists of a dual-coupler micro-ring resonator with an additional directional coupler located at the "handle" of the dumbbell structure. The reflected signal consists of traveling waves from various reflection and resonant paths (see Fig. 2.2) within the dumbbell structure.

For example, for one reflection path, which is shown in Fig. 2.2a, the input light injected into the port on the left is coupled to a counter-clockwise wave via directional coupler 1. After propagating through waveguide L_2, where L_2 is also the length of waveguide, the light is coupled into a clockwise wave via directional coupler 2 and propagates through the length of waveguide L_4. Thus the light is coupled into a backward traveling wave via directional coupler 3, and becomes a portion of the reflected signal at the left port after passing through directional coupler 1. Figure 2.2b shows another reflection path within the device. In this case, after coupling into a clockwise traveling wave via directional couplers 1 and 2, the light propagates through the lengths of waveguide L_4, L_3, and L_2 and then passes through directional couplers 3 and 2 in sequence and becomes a portion of the reflected signal after coupling into a backward traveling wave via directional coupler 1.

There are two types of resonant path inside the dumbbell micro-ring structure. One type of resonant path enables the light to resonate inside the dumbbell with no effects from the directional couplers. For example, as shown in Fig. 2.2c, the light travels along the dumbbell micro-ring and passes

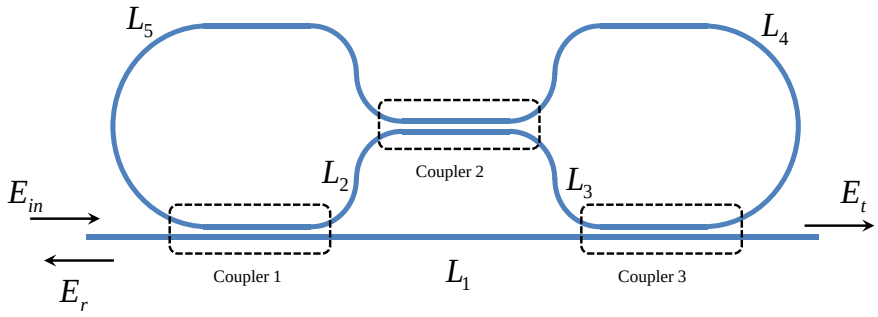

Figure 2.1: Schematic drawing of dumbbell micro-ring reflector.

through the three directional couplers and thus forms a counter-clockwise resonant wave. The other type of resonant path is shown in Fig. 2.2d as an example. The clockwise wave propagating through the left "head" of the dumbbell shape is coupled into a counter-clockwise wave via directional coupler 2. After traveling along the right "head", the wave is coupled back to a clockwise wave via directional coupler 2.

The reflected traveling waves combined with the resonant waves form the total reflected signal for the dumbbell micro-ring reflector.

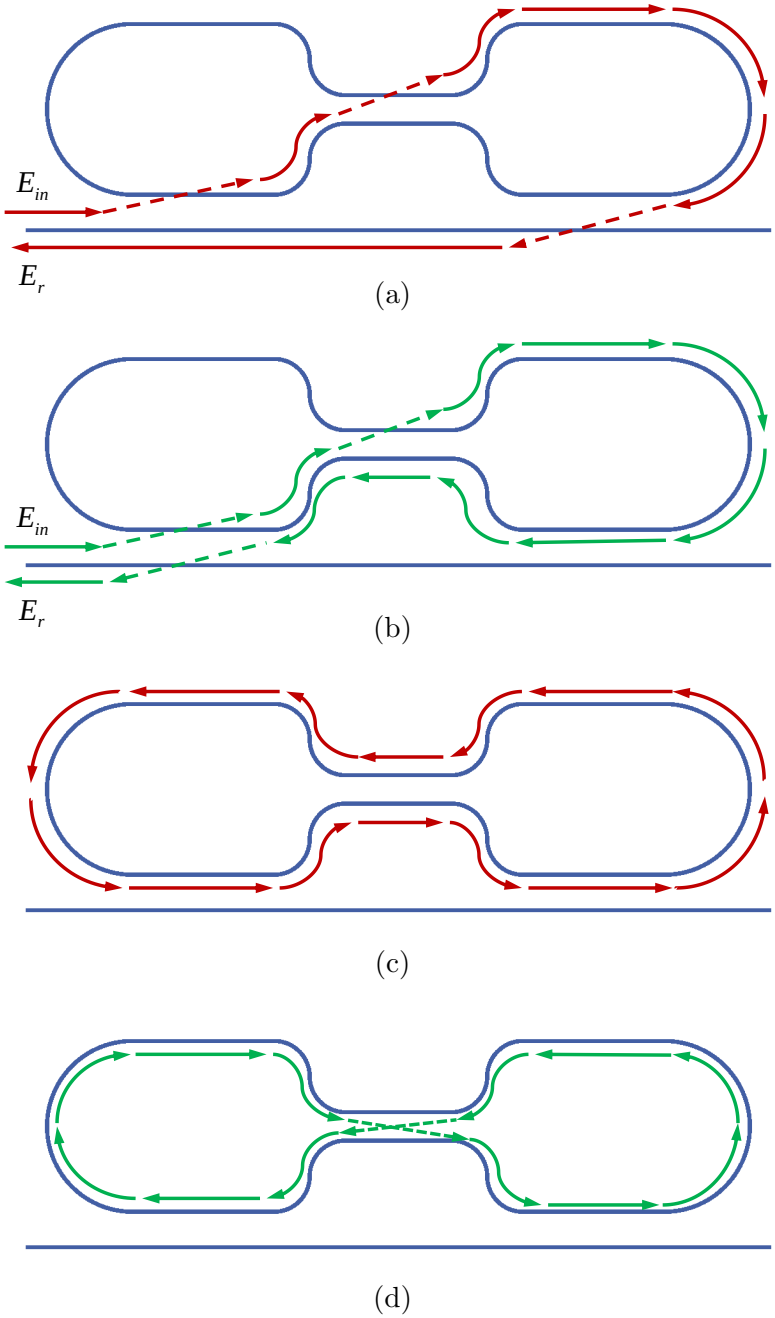

Figure 2.2: Optical paths: (a), (b): Reflection paths; (c), (d): Resonant paths.

2.2 Theoretical Analysis

2.2.1 Transfer-Matrix Method for the Directional Coupler

The coupling of optical power between two parallel waveguides occurs when the two waveguides are placed in close proximity to each other. Directional couplers, consisting of such waveguide structures, can be designed to allow certain amount of light to transfer from one waveguide to the other, depending on the design requirement. Here, we use a transfer-matrix method to model the directional couplers.

As shown in Fig. 2.3, we assume that two identical, loss-less waveguides with lengths, L, are placed near to each other with a waveguide separation, d, to allow coupling to occur. The electric field distribution of each waveguide, within the directional coupler, can be written in terms of the superposition of the even and odd eigenmodes (supermodes) of the directional coupler, which gives:

$$\begin{aligned} \psi_1(x,z) &= C_e\psi_e(x)e^{-j\beta_e\cdot z} + C_o\psi_o(x)e^{-j\beta_o\cdot z} \\ \psi_2(x,z) &= C_e\psi_e(x)e^{-j\beta_e\cdot z} - C_o\psi_o(x)e^{-j\beta_o\cdot z} \end{aligned}, \tag{2.1}$$

where $\psi_e(x)$ and $\psi_o(x)$ are the normalized even and odd mode electric fields (see Fig. 2.3a), respectively, C_e and C_o are the respective eigenmode electric field amplitudes, and β_e and β_o are the respective eigenmode propagation constants. Thus, the electric fields at the input ports of the coupler, i.e., at

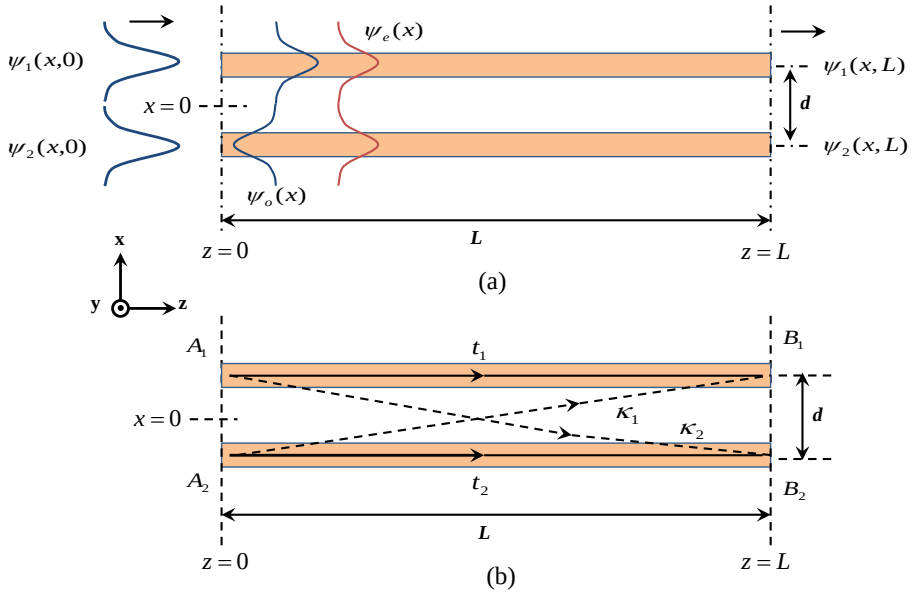

Figure 2.3: Schematic diagrams of a directional coupler

$z = 0$, can be written as:

$$\begin{aligned} \psi_1(x,0) &= C_e\psi_e(x) + C_o\psi_o(x) \\ \psi_2(x,0) &= C_e\psi_e(x) - C_o\psi_o(x) \end{aligned} . \tag{2.2}$$

After propagating along the coupler, the electric fields at the output ports, i.e., at $z = L$, can be expressed as:

$$\begin{aligned} \psi_1(x,L) &= C_e\psi_e(x)e^{-j\beta_e \cdot L} + C_o\psi_o(x)e^{-j\beta_o \cdot L} \\ \psi_2(x,L) &= C_e\psi_e(x)e^{-j\beta_e \cdot L} - C_o\psi_o(x)e^{-j\beta_o \cdot L} \end{aligned} . \tag{2.3}$$

Referring to Fig. 2.3b, the electric fields at the output ports of the coupler

can also be written in terms of the input electric fields:

$$\begin{aligned} \psi_1(x,L) &= t_1 \cdot \psi_1(x,0) + \kappa_1 \cdot \psi_2(x,0) \\ \psi_2(x,L) &= t_2 \cdot \psi_2(x,0) + \kappa_2 \cdot \psi_1(x,0) \end{aligned}, \tag{2.4}$$

where t_1 is the "straight-through" field coupling coefficient for waveguide 1, and κ_1 is the "cross" field coupling coefficient from waveguide 1 to waveguide 2. t_2 and κ_2 are the "straight-through" and "cross" coupling coefficients for waveguide 2, respectively.

Substituting Eq. (2.2) into Eq. (2.4) gives:

$$\begin{aligned} \psi_1(x,L) &= t_1[C_e\psi_e(x) + C_o\psi_o(x)] + \kappa_1[C_e\psi_e(x) - C_o\psi_o(x)] \\ \psi_2(x,L) &= t_2[C_e\psi_e(x) - C_o\psi_o(x)] + \kappa_2[C_e\psi_e(x) + C_o\psi_o(x)] \end{aligned},$$

which can be rearranged as:

$$\begin{aligned} \psi_1(x,L) &= (t_1C_e + \kappa_1C_e)\psi_e(x) + (t_1C_o - \kappa_1C_o)\kappa_o(x) \\ \psi_2(x,L) &= (t_2C_e + \kappa_2C_e)\psi_e(x) - (t_2C_o - \kappa_2C_o)\kappa_o(x) \end{aligned}. \tag{2.5}$$

Noticing that Eq. (2.5) is equivalent to Eq. (2.3), the following relationships can be obtained:

$$\begin{aligned} t_1C_e + \kappa_1C_e &= C_e e^{-j\beta_e \cdot L} \\ t_1C_o - \kappa_1C_o &= C_o e^{-j\beta_o \cdot L} \end{aligned} \quad \text{and} \quad \begin{aligned} t_2C_e + \kappa_2C_e &= C_e e^{-j\beta_e \cdot L} \\ t_2C_o - \kappa_2C_o &= C_o e^{-j\beta_o \cdot L} \end{aligned}. \tag{2.6}$$

From Eq. (2.6), the coupling coefficients can be solved as:

$$\begin{aligned} \kappa_1 = \kappa_2 &= \tfrac{1}{2}(e^{-j\beta_e \cdot L} - e^{-j\beta_o \cdot L}) \\ t_1 = t_2 &= \tfrac{1}{2}(e^{-j\beta_e \cdot L} + e^{-j\beta_o \cdot L}) \end{aligned} \tag{2.7}$$

Further simplifying Eq. (2.7) gives:

$$\begin{aligned} \kappa_1 = \kappa_2 &= -j \cdot \sin(\tfrac{\beta_e - \beta_o}{2} \cdot L) \cdot e^{-j(\frac{\beta_e + \beta_o}{2}) \cdot L} \\ t_1 = t_2 &= \cos(\tfrac{\beta_e - \beta_o}{2} \cdot L) \cdot e^{-j(\frac{\beta_e + \beta_o}{2}) \cdot L} \end{aligned} \tag{2.8}$$

Now we can redefine the "cross" and the "straight-through" field coupling coefficients as:

$$\begin{aligned} \kappa &= \sin(\tfrac{\Delta\beta}{2} \cdot L) \cdot e^{-j\beta_c \cdot L} \\ t &= \cos(\tfrac{\Delta\beta}{2} \cdot L) \cdot e^{-j\beta_c \cdot L} \end{aligned}, \tag{2.9}$$

where $\Delta\beta = \beta_e - \beta_o$ and $\beta_c = (\beta_e + \beta_o)/2$. Thus, we can express the electric fields at the output ports in terms of the electric fields at the input ports as:

$$\begin{aligned} \psi_1(x, L) &= t \cdot \psi_1(x, 0) - j\kappa \cdot \psi_2(x, 0) \\ \psi_2(x, L) &= t \cdot \psi_2(x, 0) - j\kappa \cdot \psi_1(x, 0) \end{aligned}. \tag{2.10}$$

Relabeling the ports in Fig. 2.3a to Fig. 2.3b, Eq. (2.10) is also rewritten in matrix form as:

$$\begin{bmatrix} B_1 \\ B_2 \end{bmatrix} = \begin{bmatrix} t & -j\kappa \\ -j\kappa & t \end{bmatrix} \begin{bmatrix} A_1 \\ A_2 \end{bmatrix}. \tag{2.11}$$

We would like to express A_1 and B_1 in terms of A_2 and B_2, which gives:

$$\begin{bmatrix} A_1 \\ B_1 \end{bmatrix} = \frac{1}{-j\kappa} \begin{bmatrix} -t & 1 \\ -\kappa^2 - t^2 & t \end{bmatrix} \begin{bmatrix} A_2 \\ B_2 \end{bmatrix} \tag{2.12}$$

Hence, the field components in waveguide 1, E_1, can be expressed in terms of the product of the field components in waveguide 2, E_2, and the coupling transfer-matrix, C, i.e.,

$$E_1 = CE_2, \text{where } C = \frac{1}{-j\kappa} \begin{bmatrix} -t & 1 \\ -\kappa^2 - t^2 & t \end{bmatrix} \tag{2.13}$$

2.2.2 Analytic Model of Single Ring Resonator Add-drop Filter

The transfer-matrix method is often used to investigate the optical properties of complex optical circuits. The matrix formulation can be conveniently employed to determine the transfer functions of optical resonators when multiple couplings are involved [27]. Since we will be looking at the reflection properties of the dumbbell micro-ring reflector, which consists of three directional couplers in a dumbbell shape micro-ring structure, the transfer-matrix method enables us to determine the behaviour of the device simply using the matrix manipulations, without the need for solving each reflected signal separately.

The following shows the derivation of the through port and drop port transfer functions of single ring resonator add-drop filters using the transfer-matrix method. Referring to Fig. 2.4, the single ring resonator add-drop filter consists of a micro-ring resonator with two directional couplers. The field components of the directional couplers are defined as:

$$E_i = \begin{bmatrix} a_i \\ b_i \end{bmatrix}, \quad i = 1,\ 2,\ 3,\ 4, \tag{2.14}$$

where a_i and b_i represent the field components for the waves traveling along the waveguides.

Assuming that each directional coupler consists of two identical waveguides, we define the cross-coupling coefficients for the couplers as κ_1 and κ_2 and the straight-through coupling coefficients as t_1 and t_2 (see Fig.2.4).

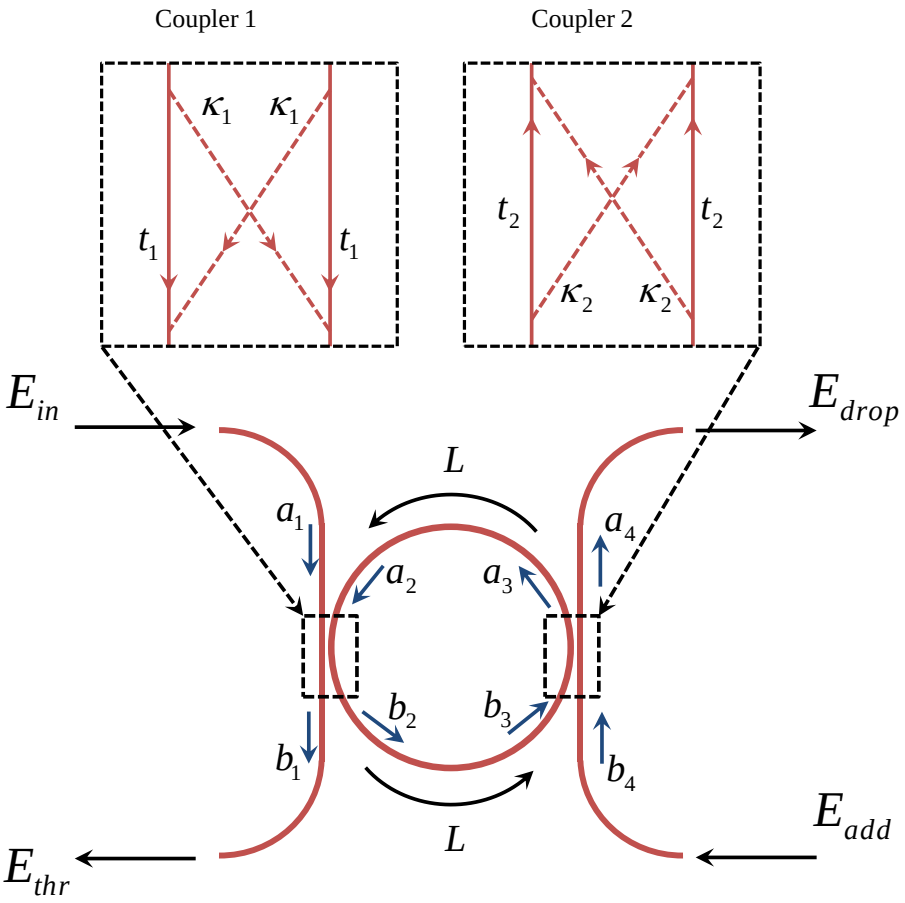

Figure 2.4: Schematic drawing of single micro-ring resonator add-drop filter.

According to Eq. (2.13), the coupling transfer-matrix of the couplers can be defined as:

$$C_m = \frac{1}{-j\kappa_m}\begin{bmatrix} -t_m & 1 \\ -t_m^2 - \kappa_m^2 & t_m \end{bmatrix}, \quad m = 1,\ 2, \tag{2.15}$$

where $\kappa_m = |\kappa_m| e^{-(j\beta_c + \alpha/2)L_C}$ and $t_m = |t_m| e^{-(j\beta_c+\alpha/2)L_C}$ are the cross field coupling and the straight-through field coupling coefficients, respectively, of the directional coupler, β_c is the propagation constant of the waveguides, as defined in Eq. (2.9), inside the coupler, and L_C is the coupling length. We note that the propagation in the micro-ring introduces phase shifts and propagation losses to the traveling waves. Hence, we define P as the propagation matrix in sections of the ring, between the couplers, of lengths, L, which can be expressed as:

$$P = \begin{bmatrix} 0 & e^{-(j\beta+\alpha/2)L} \\ e^{(j\beta+\alpha/2)L} & 0 \end{bmatrix}. \tag{2.16}$$

where β is the propagation constant of the mode of a single, unperturbed waveguide.

Using Equations (2.14), (2.15), and (2.16), the relationships between the ports of the ring can be written as:

$$\begin{bmatrix} a_1 \\ b_1 \end{bmatrix} = C_1 P C_2 \begin{bmatrix} b_4 \\ a_4 \end{bmatrix}. \tag{2.17}$$

Referring to the port labels in Fig. 2.4, Eq. (2.17) can also be written as:

$$\begin{bmatrix} E_{in} \\ E_{thr} \end{bmatrix} = C_1 P C_2 \begin{bmatrix} E_{add} \\ E_{drop} \end{bmatrix} \equiv M \begin{bmatrix} E_{add} \\ E_{drop} \end{bmatrix} \equiv \begin{bmatrix} M_{1,1} & M_{1,2} \\ M_{2,1} & M_{2,2} \end{bmatrix} \begin{bmatrix} E_{add} \\ E_{drop} \end{bmatrix} \quad (2.18)$$

where the matrix M is the transfer matrix of the device.

Assuming that the light is only injected from the input port, i.e., $a_1 = E_{in}$ and $b_4 = E_{add} = 0$, the transfer functions, for the power, of the through and drop ports are given by:

$$G_{thr} = \frac{|E_{thr}|^2}{|E_{in}|^2} = \frac{|M_{2,2}|^2}{|M_{1,2}|^2} \quad (2.19)$$

$$G_{drop} = \frac{|E_{drop}|^2}{|E_{in}|^2} = \frac{1}{|M_{1,2}|^2} \quad (2.20)$$

The transfer functions in Equations (2.19) and (2.20) show the convenience and simplicity of using the transfer-matrix method to characterize the transmission and reflection properties of optical circuits. Thus, we will analyze and characterize our device using this approach.

2.2.3 Analytic Model of Dumbbell Micro-ring Reflector

The transfer-matrix method, introduced in the previous section, has been used to analyze the reflection properties of our device. The field components of the directional couplers are defined as:

$$E_i = \begin{bmatrix} a_i \\ b_i \\ c_i \\ d_i \end{bmatrix}, \quad i = 1,\ 2,\ 3, ...,\ 6, \tag{2.21}$$

where a_i and b_i represent the field components for the forward traveling waves along the waveguides and c_i and d_i represent the field components for the backward traveling waves (see Fig. 2.5).

Assuming that there is no mixing between the forward and backward traveling waves, we can express the coupling relationships for both the forward and backward traveling waves within the directional coupler using a 4×4 coupling matrix[6, 13]:

$$C = \frac{1}{-j\kappa} \begin{bmatrix} -t & 1 & 0 & 0 \\ -t^2 - \kappa^2 & t & 0 & 0 \\ 0 & 0 & -t & 1 \\ 0 & 0 & -t^2 - \kappa^2 & t \end{bmatrix}, \tag{2.22}$$

where $\kappa = |\kappa| e^{-(j\beta_c + \alpha/2)L_C}$ and $t = |t| e^{-(j\beta_c + \alpha/2)L_C}$ are the cross field coupling and the straight-through field coupling coefficients, respectively, of the directional coupler, β_c is the propagation constant of the waveguides inside

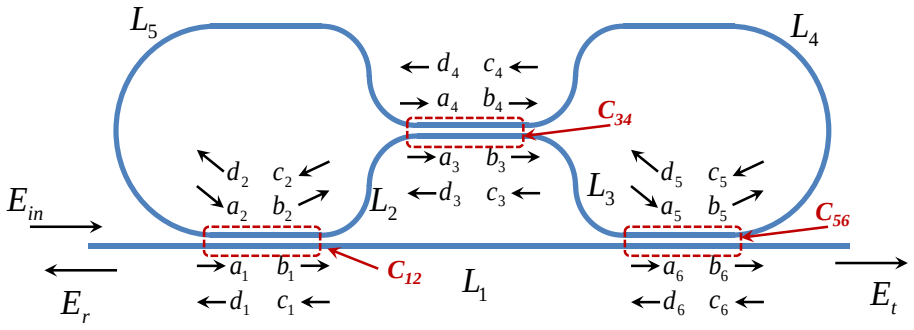

Figure 2.5: 2D schematic drawing of dumbbell micro-ring reflector with device dimensions, field components, and couplers labeled.

the coupler, α is the propagation loss coefficient, and L_C is the coupling length. Within one directional coupler, the power transmission ratio, T_C, can be expressed as $T_C = |\kappa|^2 + |t|^2$. Using Equations (2.21) and (2.22), the field components within each directional coupler can be expressed as:

$$E_1 = C_{12}E_2,\ E_3 = C_{34}E_4,\ \text{and}\ E_5 = C_{56}E_6 \tag{2.23}$$

where C_{12}, C_{34}, and C_{56} (see Fig. 2.5) are the coupling matrices, respectively, between the fields E_i and E_{i+1} ($i = 1,\ 3,\ \text{and}\ 5$) within the directional couplers.

We define P_m ($m = 1,\ 2, ...,\ 5$) to be the propagation transfer matrices for light propagating through the length of waveguides L_m between the directional couplers. The propagation matrix, for each waveguide that bridges

the directional couplers, is given by

$$P_2 = \begin{bmatrix} 0 & 0 & 0 & 0 \\ P_{L_2}^{-1} & 0 & 0 & 0 \\ 0 & 0 & 0 & P_{L_2} \\ 0 & 0 & 0 & 0 \end{bmatrix} \quad P_3 = \begin{bmatrix} 0 & P_{L_3} & 0 & 0 \\ 0 & 0 & 0 & 0 \\ 0 & 0 & P_{L_3}^{-1} & 0 \\ 0 & 0 & 0 & 0 \end{bmatrix}$$
$$P_4 = \begin{bmatrix} 0 & 0 & 0 & 0 \\ 0 & 0 & P_{L_4}^{-1} & 0 \\ 0 & P_{L_4} & 0 & 0 \\ 0 & 0 & 0 & 0 \end{bmatrix} \quad P_5 = \begin{bmatrix} 0 & 0 & 0 & P_{L_5} \\ 0 & 0 & 0 & 0 \\ 0 & 0 & 0 & 0 \\ P_{L_5}^{-1} & 0 & 0 & 0 \end{bmatrix} \tag{2.24}$$

where $P_{L_m} = e^{-(j\beta+\alpha/2)L_m}$. The relationships of the field components between the couplers are thus give by

$$E_2 = P_2E_3 + P_5E_4 \text{ and } E_5 = P_3E_3 + P_4E_4 \tag{2.25}$$

Using Equations 2.23 and 2.25, the relationship between the left port and the right port of the device is given by

$$E_1 = C_{12}(P_2C_{34} + P_5)(P_3C_{34} + P_4)^{-1}C_{56}E_6. \tag{2.26}$$

Since the transfer matrices in Eq. (2.26) are 4×4 matrices, the result of the multiplication of transfer matrices can also be written in terms of an

equivalent 4×4 matrix M, i.e.

$$M = C_{12}(P_2 C_{34} + P_5)(P_3 C_{34} + P_4)^{-1} C_{56} \tag{2.27}$$

Substituting the field components defined in Eq. (2.21) into Eq. (2.26), we can express Eq. (2.26) as:

$$\begin{bmatrix} a_1 \\ b_1 \\ c_1 \\ d_1 \end{bmatrix} = \begin{bmatrix} M_{1,1} & \cdots & M_{1,4} \\ \vdots & \ddots & \vdots \\ M_{4,1} & \cdots & M_{4,4} \end{bmatrix} \begin{bmatrix} a_6 \\ b_6 \\ c_6 \\ d_6 \end{bmatrix} \tag{2.28}$$

where $M_{i,j}$ represents the elements in matrix M.

Assuming that light is only injected into the left port, i.e., the input signal $a_1 = E_{in}$ and $c_6 = 0$, and knowing that the connection between the two couplers via waveguide L_1 can be expressed as:

$$a_6 = P_{L_1} b_1 \text{ and } d_6 = P_{L_1}^{-1} c_1. \tag{2.29}$$

Thus, we can rewrite Eq. (2.28) as:

$$\begin{bmatrix} a_1 \\ b_1 \\ c_1 \\ d_1 \end{bmatrix} = \begin{bmatrix} M_{1,1} & \cdots & M_{1,4} \\ \vdots & \ddots & \vdots \\ M_{4,1} & \cdots & M_{4,4} \end{bmatrix} \begin{bmatrix} P_{L_1} b_1 \\ b_6 \\ 0 \\ P_{L_1}^{-1} c_1 \end{bmatrix}. \tag{2.30}$$

We can solve Eq. (2.30) and express the field components b_1 and b_6 in

terms of c_1:

$$b_1 = \frac{M_{2,2} + (M_{3,2}M_{2,4} - M_{2,2}M_{3,4})P_{L_1}^{-1}}{M_{3,2} + (M_{2,2}M_{3,1} - M_{3,2}M_{2,1})P_{L_1}} \cdot c_1 \tag{2.31}$$

and

$$b_6 = \frac{1 - M_{3,4}P_{L_1} - \frac{M_{3,1}P_{L_1}[M_{2,2} + (M_{3,2}M_{2,4} - M_{2,2}M_{3,4})P_{L_1}]}{M_{3,2} + (M_{2,2}M_{3,1} - M_{3,2}M_{2,1})P_{L_1}}}{M_{3,2}} \cdot c_1. \tag{2.32}$$

Substituting Eq. (2.31) and Eq. (2.32) into Eq. (2.30), we can calculate the reflectivity of the device:

$$R = \frac{|E_r|^2}{|E_{in}|^2} = \left|\frac{d_1}{a_1}\right|^2 = \frac{M_{4,1}P_{L_1} \cdot r_1 + M_{4,2} \cdot r_2 + M_{4,4}P_{L_1}^{-1}}{M_{1,1}P_{L_1} \cdot r_1 + M_{1,2} \cdot r_2 + M_{1,4}P_{L_1}^{-1}} \tag{2.33}$$

where r_1 and r_2 are the ratios of the field components b_1 and b_6 to c_1 respectively, i.e.,

$$r_1 = \frac{b_1}{c_1} = \frac{M_{2,2} + (M_{3,2}M_{2,4} - M_{2,2}M_{3,4})P_{L_1}^{-1}}{M_{3,2} + (M_{2,2}M_{3,1} - M_{3,2}M_{2,1})P_{L_1}} \tag{2.34}$$

and

$$r_2 = \frac{b_6}{c_1} = \frac{1 - M_{3,4}P_{L_1} - \frac{M_{3,1}P_{L_1}[M_{2,2} + (M_{3,2}M_{2,4} - M_{2,2}M_{3,4})P_{L_1}]}{M_{3,2} + (M_{2,2}M_{3,1} - M_{3,2}M_{2,1})P_{L_1}}}{M_{3,2}}. \tag{2.35}$$

2.3 Simulation

In this section, we present the simulations of the reflection properties of the dumbbell micro-ring reflector, based on the analytic model described in previous section, to verify our design approach. We defined the geometry of the SOI photonic waveguide and calculated its effective refractive index and group index for a single TE mode using a 2-D Finite-Difference eigenmode solver[8, 19]. We then used a curve-fitting model, introduced by Rouger et al.[14], to calculate the coupling lengths of the couplers, which give us the required coupling coefficients, for our device. In Sections 2.3.3 and 2.3.4, we investigated the effects of the coupling coefficients, which determine our device performance, and then optimized our design based on numerical simulations in MATLAB.

Table 2.1 lists the definitions of the parameters that were used in our simulation.

Symbol	Significance	Unit
α	Propagation loss	/m
β	Propagation constant	rad/cm
κ	Cross-coupling coefficient	
t	Straight-through coupling coefficient	
λ	Optical wavelength	nm
n_{eff}	Effective refractive index	
n_g	Group refractive index	
L_C	Coupling length	μm
G	Coupler gap distance	nm
T_C	Power transfer ratio	

Table 2.1: List of Simulation Parameters.

2.3.1 Silicon-on-Insulator Strip Waveguides

We designed the dumbbell shape micro-ring reflector based on 500-nm-wide, 220-nm-high, silicon photonic nano-wires laying on top of a silicon dioxide layer which has a thickness greater than 1 μm (see Fig. 2.6a). The high refractive index contrast between silicon and silicon dioxide enables strong confinement of the optical mode[3]. The waveguide geometry was chosen to ensure single mode propagation for TE polarization, while still having low propagation loss[3].

Assuming that the ambient temperature was 25°C, we calculated the waveguide effective refractive index, n_{eff}, using a 2-D Finite-Difference eigenmode solver[8, 19]. This eigenmode solver calculates the optical modes of the waveguide by solving Maxwell's equations on a cross-sectional mesh of the waveguide using a finite difference algorithm, assuming that the waveguide is infinitely long along the direction of propagation and its cross-section is invariant. n_{eff}, as shown in Fig. 2.6b, is wavelength dependent. Hence, the propagation constant of the guided mode at a single wavelength can be calculated as $\beta = 2\pi n_{eff}/\lambda$.

Given that n_{eff} is highly dispersive, the group index, n_g, was used in our calculation of the optical phase for predicting the resonator's free spectrum range. We calculated n_g using the equation[27]

$$n_g = n_{eff} - \lambda \frac{dn_{eff}}{d\lambda}, \tag{2.36}$$

in our simulations.

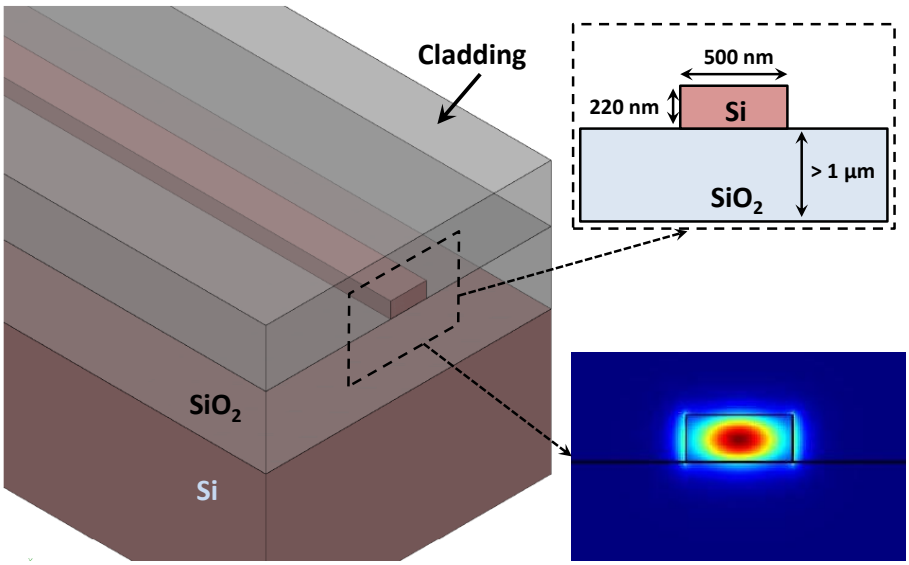

(a)

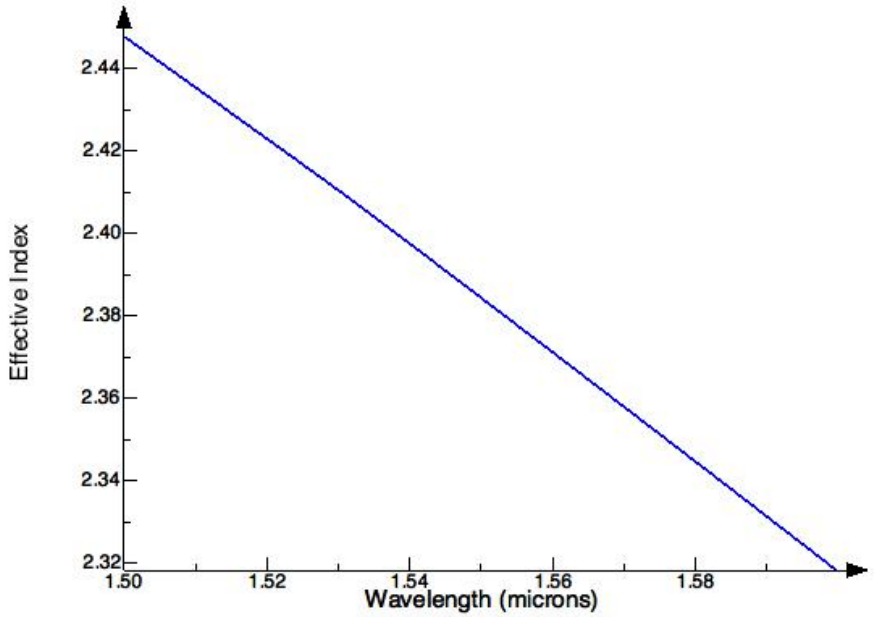

(b)

Figure 2.6: (a) Perspective view of SOI strip waveguide with insets showing the waveguide geometry and TE mode distribution; (b) Wavelength-dependent effective index of SOI strip waveguide.

2.3.2 Directional Coupler

In our device, the directional coupler consists of two identical parallel-coupled SOI waveguides with 200 nm gap distance (see Fig. 2.7). The power behavior within a directional coupler can be expressed as a function of the structure of the coupler, the position in the coupler, the coupling coefficients, and the power transmission ratio[14]. The field coupling coefficients, κ and t, can be expressed as:

$$\begin{aligned} \kappa^2 &= \sin^2\left(B \cdot L_C \cdot e^{-A \cdot G}\right) \\ t^2 &= \cos^2\left(B \cdot L_C \cdot e^{-A \cdot G}\right) \end{aligned} \tag{2.37}$$

where A and B are coefficients obtained by curve-fitting the exponential behavior of the coupling coefficients as functions of the coupler gas distance, G, and coupling length, L_C[14]. In this case, given G, κ, and the power transmission ratio, T_C, we can calculate L_C from the following equation:

$$L_C = \arcsin\left(\frac{|\kappa|}{\sqrt{T_C}}\right) \cdot \left(B \cdot e^{-A \cdot G}\right)^{-1}, \tag{2.38}$$

where $A = 9.0842834 \cdot 10^{-3}$ nm^{-1} and $B = 1.8670660 \cdot 10^{-4}$ nm^{-1} are extracted from Ref. 14 at $T = 298K$ and $\lambda = 1550$ nm. In our simulation, we assume that the coupling between the straight waveguide and the ring structure is only due to the coupling between the parallel section of the coupler.

Since β_c, defined in Equations (2.9), (2.15), and (2.22) is given by $\beta_c =$

$(\beta_e + \beta_o)/2$, we can calculate β_c using:

$$\beta_c = \frac{2\pi}{\lambda} \cdot n_c = \frac{2\pi}{\lambda} \cdot (\frac{n_e + n_o}{2})$$

where n_e and n_o are the effective indices of the even and odd modes of the directional coupler, respectively, and n_c is taken to be the effective index of the directional coupler and is equal to the average of the even and odd mode effective indices. n_e and n_o can be calculated using the 2-D FD mode solver and, thus, n_c can be obtained. As shown in Fig. 2.8, n_c (labeled as Neff_c) is approximately equal to the effective index of a single, unperturbed waveguide, n_{eff} (labeled as Neff_SWG), i.e., $n_c \approxeq n_{eff}$. Hence, $\beta_c \approxeq \beta$, where β is the propagation constant of a single, unperturbed waveguide. From now on we use β as the propagation constant for the waveguides inside and outside of the directional couplers in our simulations.

To take the real situation into account, we also include waveguide propagation loss and coupling loss in our transfer-matrix equation. We use a waveguide power propagation loss of $\alpha_{[/m]} = 115.12/\text{m}$, converted from $\alpha_{[\text{dB}/cm]} = 5$ dB/cm. We use a power transmission ratio of $T_C = 0.9$, which is based on our fabrication and measurement experience, in our simulations. Therefore, the straight-through coupling coefficients t can be expressed as

$$t = \sqrt{0.9 - |\kappa|^2} \cdot e^{-(j\beta + \alpha/2)L_C}. \tag{2.39}$$

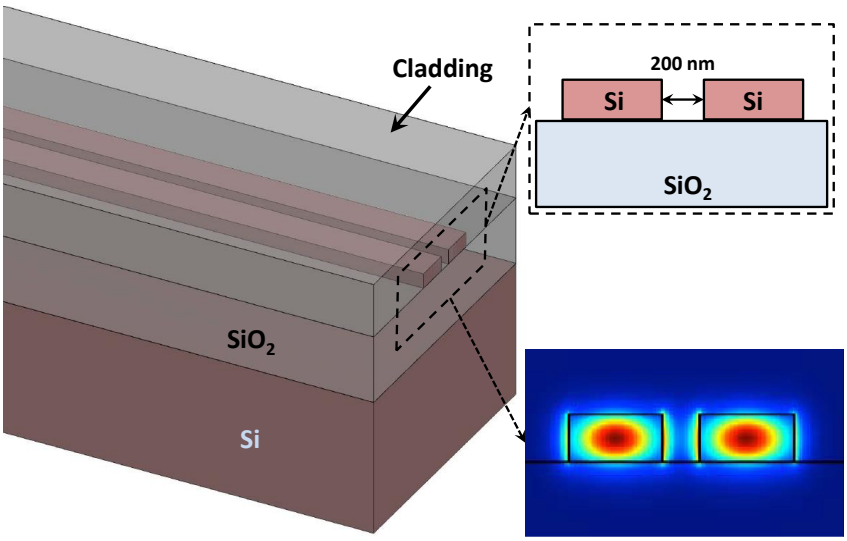

Figure 2.7: Perspective view of directional coupler with gap distance labeled and an inset showing symmetric TE mode distribution profile.

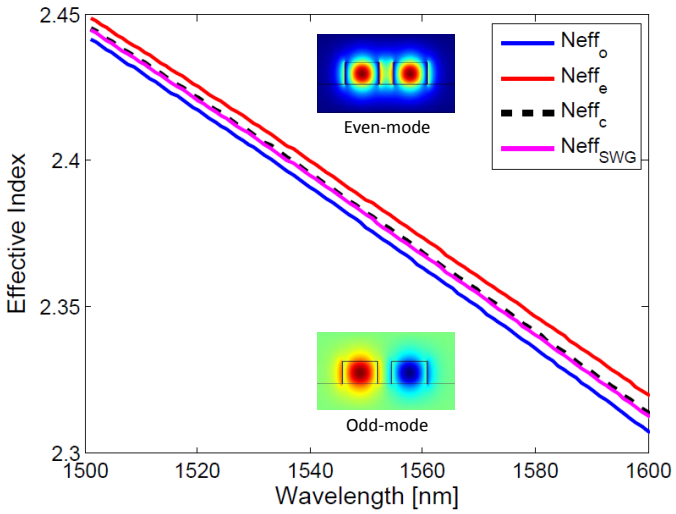

Figure 2.8: Effective indices of the even and odd modes in directional coupler and the effective index of a single waveguide, with insets showing the even and odd TE mode electric field distributions of the directional couplers.

2.3.3 Effects of Coupling Coefficients

Referring to the parameters defined in Equations (2.22), (2.24), (2.36), (2.38), and (2.39), and substituting them into Eq. (2.33), the reflectivity of the device, R, can be expressed as a function of wavelength and the magnitudes of the cross-coupling coefficients of the three directional couplers of the device, i.e.,

$$R = f(\lambda, |\kappa_{12}|, |\kappa_{34}|, |\kappa_{56}|). \tag{2.40}$$

Hence, the cross-coupling coefficients, κ_{12}, κ_{34}, and κ_{56}, of the device are key factors in determining the performance of the dumbbell micro-ring reflector and, as shown in Fig. 2.9, can significantly affect the magnitude of the reflectivity spectrum as well as the values of the free spectral range and the quality factor. The curves in Fig. 2.9 indicate that the reflectivity spectrum with different selections of the three coupling coefficients may have either high reflectivity with high extinction ratio, or high reflectivity with low extinction ratio, or low reflectivity with high extinction ratio, or low reflectivity with low extinction ratio. Since the device is designed for use as a reflector, the reflection spectrum should have high reflectivity with high extinction ratio. In this case, κ_{12}, κ_{34}, and κ_{56} should be carefully chosen to meet this requirement.

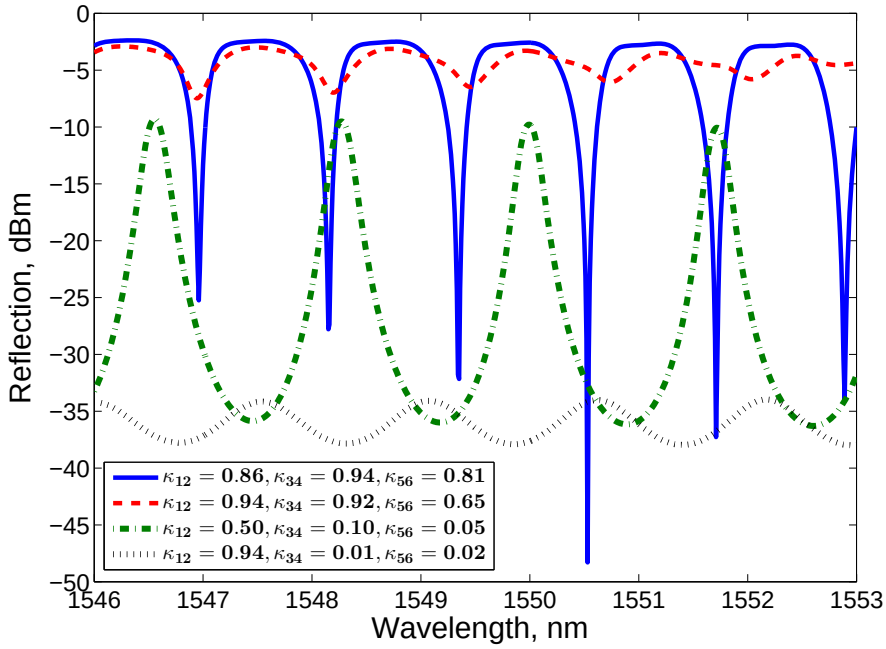

Figure 2.9: Simulated reflectivity responses for several sets of coupling coefficients that give (a) high reflectivity, high extinction ratio, or (b) high reflectivity, low extinction ratio, or (c) low reflectivity, high extinction ratio, or (d) low reflectivity, low extinction ratio[30]. Copyright 2012 Society of Photo-Optical Instrumentation Engineers.

2.3.4 Design Optimization

To optimize the performance of the reflector, we need to find the proper values for the coupling coefficients of our device. In this case, we define R_p to be the maximum reflectivity and R_v to be the minimum reflectivity for the various possible combinations of cross-coupling coefficients of the three couplers. We scan the reflection spectrum and calculate the reflectivity difference $R_p - R_v$ and the reflectivity extinction ratio $10\log_{10}(R_p/R_v)$ as functions of the three cross-coupling coefficients of the couplers.

The simulation results are shown in Fig. 2.10 and Fig. 2.11 using hot colormaps, where brighter colors correspond to higher values. Figure. 2.10 shows the simulation results of the reflectivity differences as a function of $|\kappa_{12}|$, $|\kappa_{34}|$, and $|\kappa_{56}|$, and Figure. 2.11 shows the simulation results of the reflectivity extinction ratio as a function of $|\kappa_{12}|$, $|\kappa_{34}|$, and $|\kappa_{56}|$. Based on our simulation results, we choose the values for the three cross-coupling coefficients, which are $|\kappa_{12}| = 0.84$, $|\kappa_{34}| = 0.94$, and $|\kappa_{56}| = 0.77$, to meet the requirements of high reflectivity and high extinction ratio.

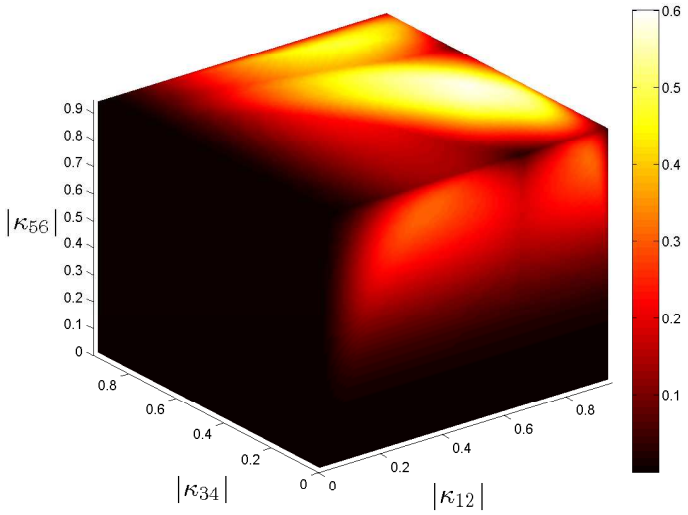

(a)

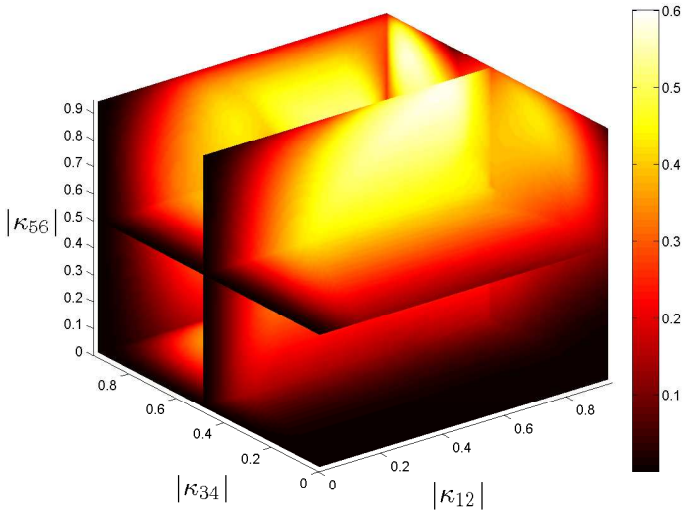

(b)

Figure 2.10: Reflectivity differences as functions of κ_{12} , κ_{34}, and κ_{56}: (a) Perspective volume view; (b) Perspective view with cross-sectional slices.

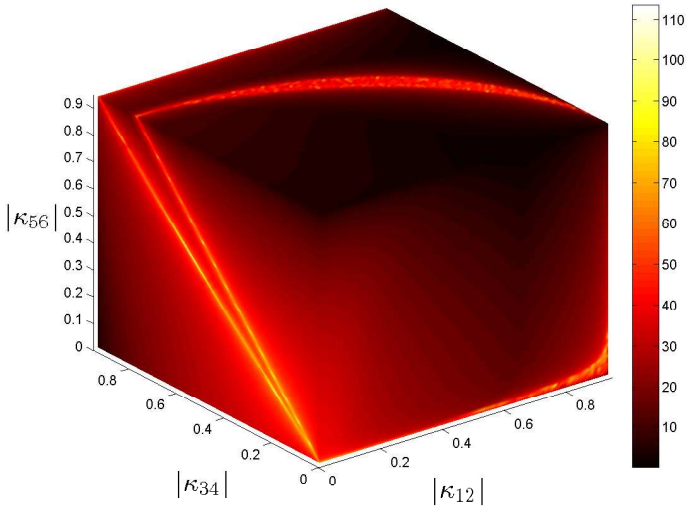

(a)

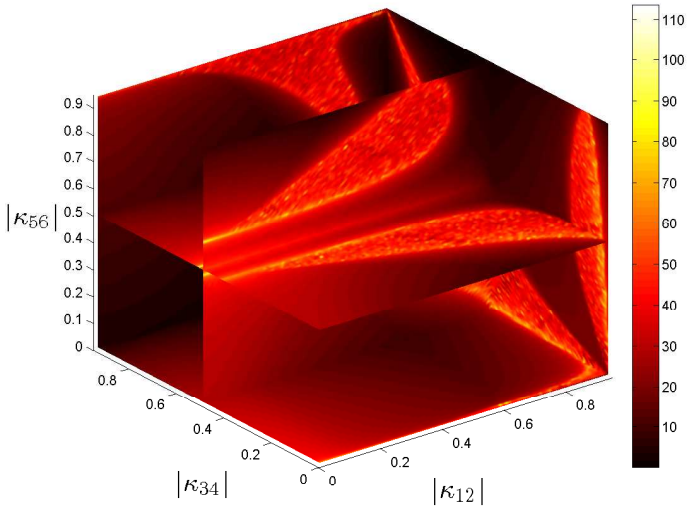

(b)

Figure 2.11: Reflectivity extinction ratios as functions of κ_{12} , κ_{34}, and κ_{56}: (a) Perspective volume view; (b) Perspective view with cross-sectional slices.

Chapter 3

Automated Optical Measurement System

To characterize fabricated devices, an automated optical measurement setup has been developed for measuring on-chip nanophotonic circuits. This automated system has been designed to perform high speed and high resolution wavelength-swept measurements with accurate fibre alignment. In this chapter, we introduce the hardware setup as well as the system operation of the automated setup. Measurement results of a strip waveguide are also presented to show the system performance including system stability, measurement repeatability, and measurement flexibility.

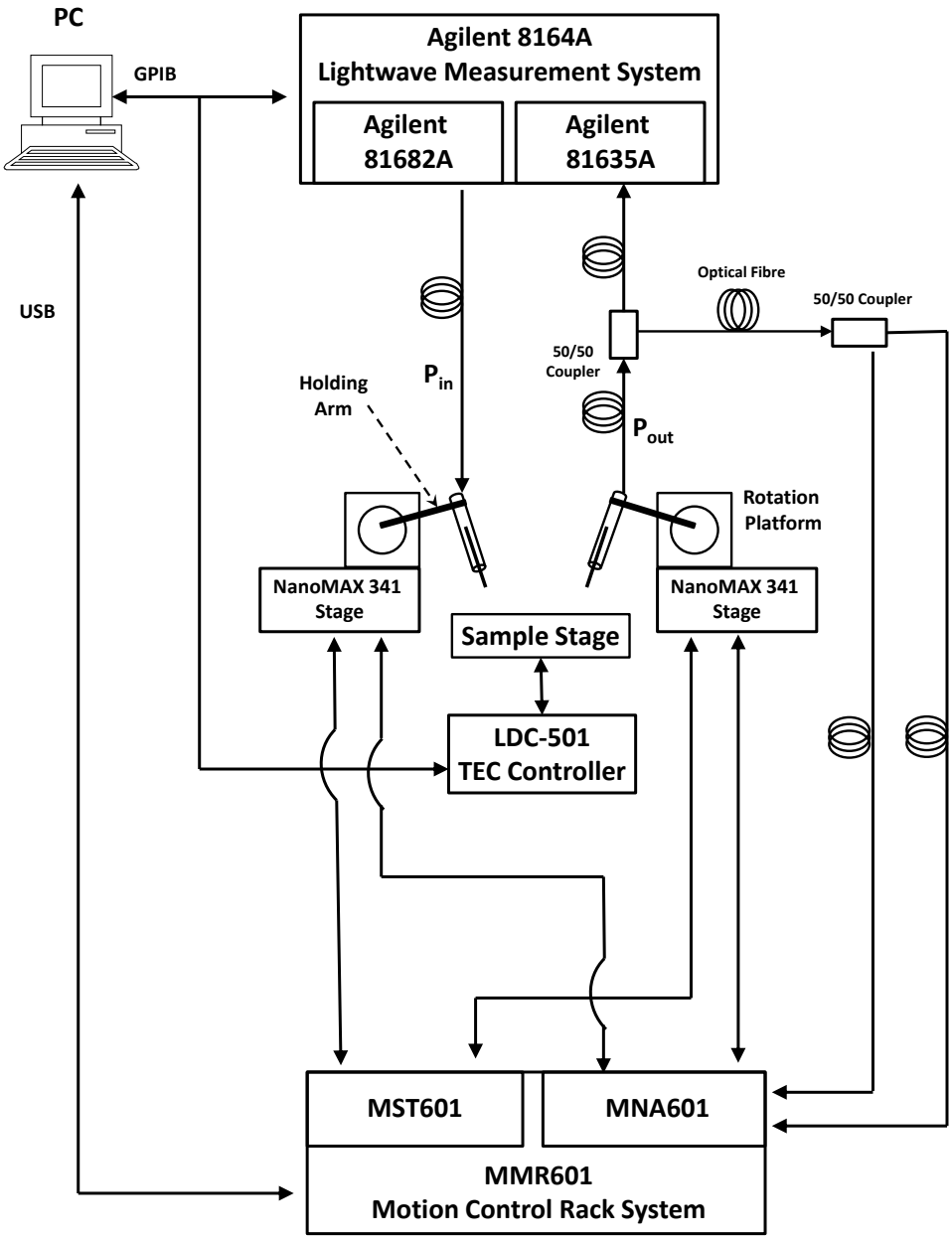

Figure 3.1: Schematic diagram of automated measurement system.

3.1 Fibre-to-Fibre Automated Measurement Setup

We have developed an automated optical probe station for characterizing on-chip nanophotonic circuits. We assembled the entire measurement setup on top of an optical table, supported by pneumatic vibration isolators with automatic re-leveling, to minimize environmental disturbances during the measurements. The schematic diagram of the automated probe station, as shown in Fig. 3.1, consists of two sets of micro/nano-positioners independently controlled to position two optical fibres (input and output), a motion control rack system, a sample stage with temperature control, a tunable laser system, and other peripherals to measure the optical responses of the devices. This measurement system has been modularized so that its subsystems can be extended and changed easily for innovative experiments. Figure 3.2 shows the implemented setup.

3.1.1 Nano-positioned Optical Probes

In the setup, two side-loading fibre chucks[25], installed with two cleaved optical fibres, were used as the input and output probes. The fibre chucks, as shown in Fig. 3.2 ①, were held by two aluminum arms. These arms were installed, respectively, on two rotation platforms that were mounted to the automated stages via aluminum adapter plates. The aluminum arms and adapter plates were custom-designed using 3D CAD software to fit other hardware components (see Fig. 3.3). The rotation platforms gave flexibility for tuning the incident angle of the probes from 0° to 90° by rotating the

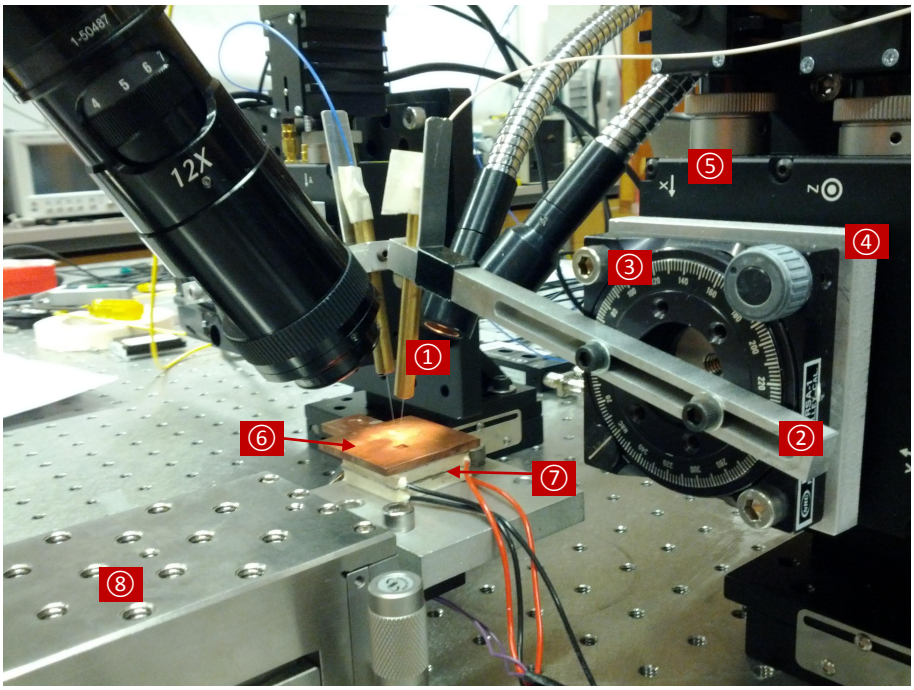

Figure 3.2: Automated optical probe station setup with parts labeled: ① Fibre chuck; ② Holding arm; ③ Rotation platform; ④ Adapter plate; ⑤ MAX341 Stage; ⑥ Heat sink; ⑦ Thermoelectric cooler; ⑧ Sample stage.

holding arms, which helps to maximize the coupling efficiency and to match the grating peak transmission wavelength.

The probe motions were automated by two NanoMax MAX341 stages[26] which give sub-micron resolution positioning to accurately align the input/output fibres to the periodic grating couplers integrated on the chip. The NanoMax MAX341 stages, purchased from Thorlabs, Inc., are 3-axis flexure stages with a stepper motor and a closed-loop internal piezoelectric actuator on each axis. The stepper motors are able to provide the stage 4mm-travel-distance per axis with 0.06 μm minimum step size, an accuracy

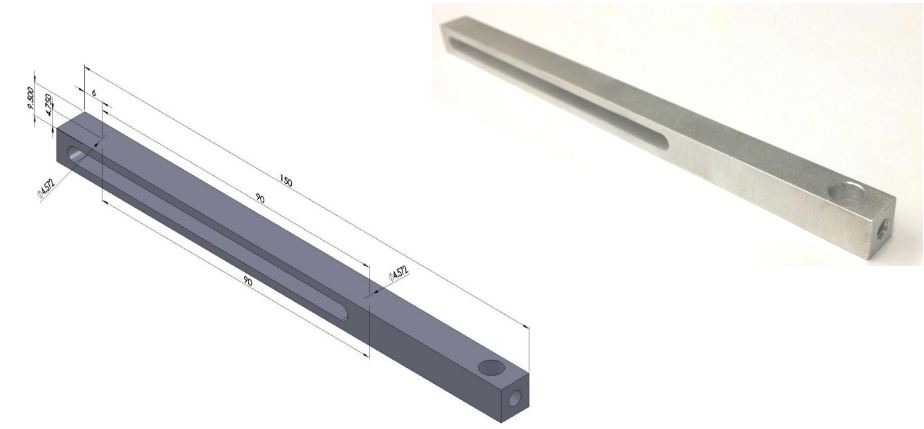

(a)

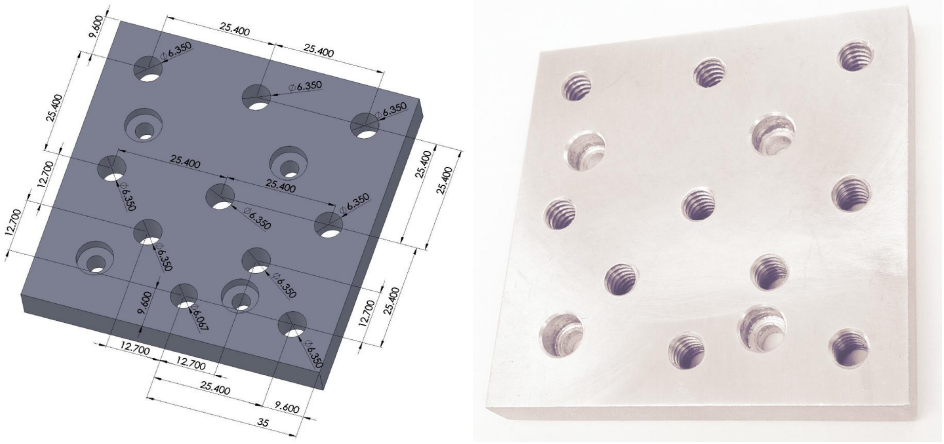

(b)

Figure 3.3: Custom-designed mechanical components: (a) 3D CAD model and manufactured arm; (b) 3D CAD model and manufactured adapter plate.

of 1.0 μm, a repeatability of 0.5 μm, and a backslash of <7 μm. The closed-loop internal piezoelectric actuators give the stages 20 μm travel range with a positional resolution of 20 nm on each axis.

3.1.2 Motion Control Rack System

The automated stages were driven and controlled by an APT^{TM} MMR601 Rack System[24] containing three plug-in dual-channel stepper motor controller modules (MST601) and two plug-in Nanotrak control modules (MNA601). The rack system was connected to the computer via a USB cable. The three MST601 modules, which contain six channels in total, were connected, respectively, to the stepper motors of the two NanoMax MAX341 stages. The two MNA601 modules were connected to the output fibre via single-mode fibres and 50/50 benchtop couplers for fibre auto-alignment. Connecting to the motorized stages, the MNA601 modules drove the built-in piezoelectric actuators through coaxial SMC cables and received the feedback signals through 7-pin LEMO cables for closed-loop piezoelectric actuation.

3.1.3 Sample Stage with Thermal Control System

We used a 3-axis linear translation manual stage as the sample stage that held our optical chips. We attached a thermoelectric cooler and a thermistor to a copper heat sink using thermal adhesive. The copper heat sink was mounted to the sample stage. The thermoelectric cooler and the thermistor were connected to the TEC controller module of the Stanford Research Systems LDC-501. The LDC-501 maintained the copper heat sink at a stabilized operating temperature and was able to be program-controlled by

the computer via a GPIB (General Purpose Interface Bus) connection.

3.1.4 Tunable Laser System

For the tunable laser system, we used an Agilent 8164A Lightwave Measurement System mainframe[23] with an Agilent 81682A tunable laser source (TLS) module[21] and an Agilent 81635A power sensor module[22] installed. The Agilent 81628A TLS module covered the wavelength range from 1460 nm to 1580 nm, and provided up to 8 dBm of power with a wavelength resolution of 0.1 pm. The built-in wavelength meter of the TLS module provided a wavelength accuracy of ±10 pm, which was necessary to accurately and reproducibly characterize the devices. The Agilent 81635A power sensor measured the power in the wavelength range from 800 nm to 1650 nm over a power range from +10 dBm to -80 dBm. The Agilent 8164A mainframe communicated with the computer via a GPIB connection and controlled both the TLS module and the power sensor during wavelength-swept measurements.

3.1.5 Monitoring System

A monitoring system, including microscope and CMOS USB camera, was also implemented to simultaneously view the input/output fibre alignment. The camera, which was attached to the microscope, was connected to the computer and the video is displayed on the computer monitor.

3.2 System Operation

3.2.1 Measurement Principle

The input optical fibre, connected to the output the TLS module, was moved by the motorized NanoMax MAX341 stage to inject light into the input port of the optical circuits. The optical responses of the device were collected by the output fibre, and were then split into two identical signals via a 50/50 benchtop coupler connected to the output fibre. One of the two signals is delivered to the power sensor module for wavelength-swept measurements. The other signal was split, again, into two identical signals by a second 50/50 benchtop coupler. These two signals, with one quarter of the output power in each of them, were delivered, respectively, to the two MNA601 modules of the rack system for auto-alignment.

The plugged-in MNA601 modules installed in the MMR601 main rack system were provided with ActiveX control components from Thorlabs, Inc. Each ActiveX control component provided a graphical user interface (GUI) and a programmable interface. We integrated all of the ActiveX control components of the control modules into a system control GUI [11]. This GUI, as shown in Fig. 3.4, integrates the functionalities from both the MST601 modules and the MNA601 modules and thus enables us to control the movements of the automated stage and to perform the embedded fibre auto-alignment function.

The system control GUI was developed and programmed by Charlie Lin using Matlab.

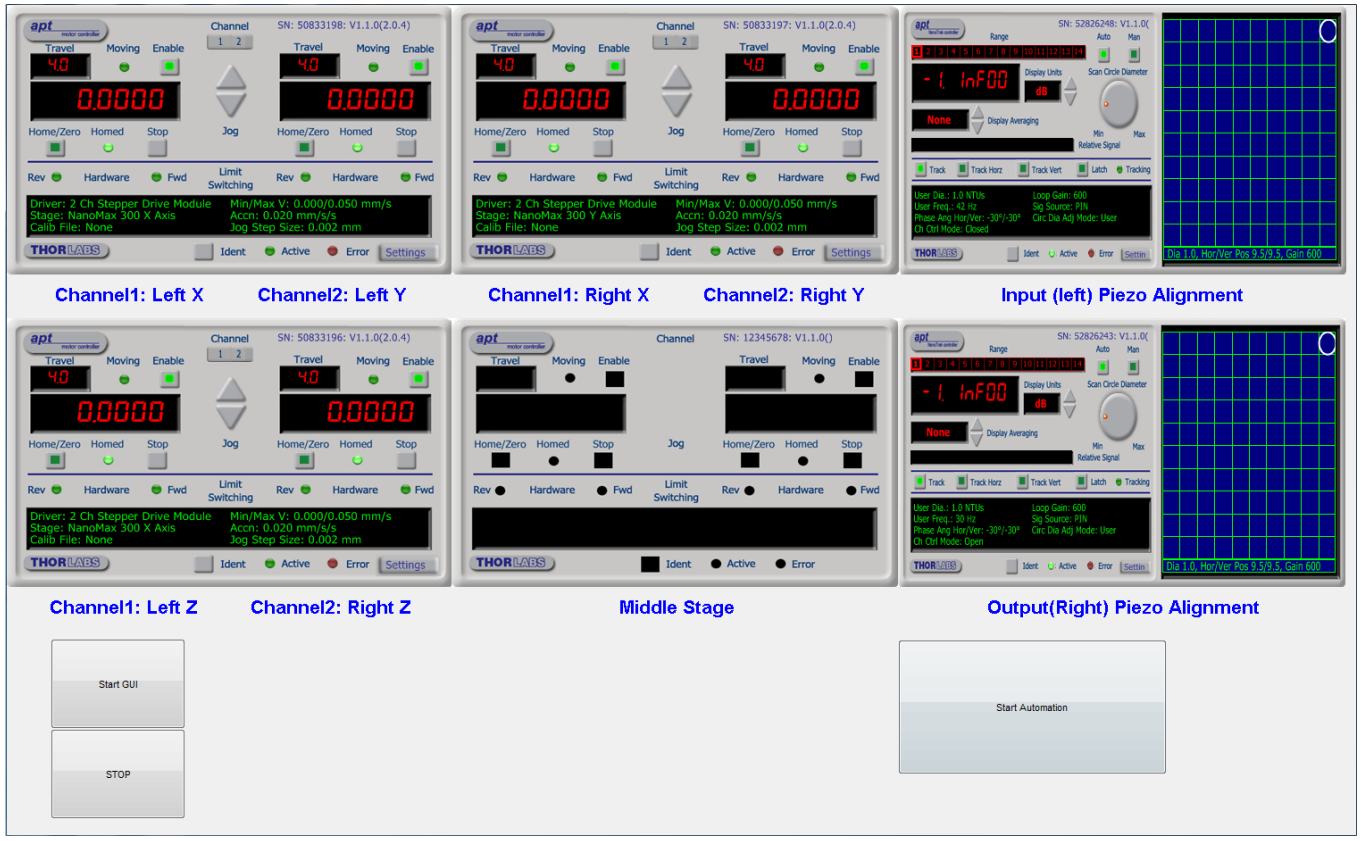

Figure 3.4: System control GUI.

3.2.2 Operation Modes

As shown in Fig. 3.5, the setup supports two operation modes, fully-automatic mode and semi-automatic mode. To start with, for each mode, we initialize the system GUI and move all of the motors to their "Home" positions, which are set during manufacture and taken to be the zero offset positions. The system GUI then establishes a horizontal coordinate system for each stage, which uses the "Home" position and the 4mm×4mm travel range of the stage as the origin and the first quadrant, respectively, of the coordinate system. We call the coordinates in this coordinate system as "motor coordinates", which give the distances that the motorized stages need to move to the required positions.

We use fully-automatic mode to characterize multiple on-chip optical devices having constant input/output fibre incident angles. The measurements in fully-automatic mode require the motor coordinates of the integrated grating couplers of the devices to automatically align the input/output fibres. In this case, we align the input/output fibres to the grating couplers of the first device using piezoelectric auto-alignment and save the corresponding motor coordinates of the stages in the system GUI. We then move the fibres and repeat the above procedures on the last device. We extract the coordinates of the grating couplers of all of the devices from the mask layout GDS file, and save them in an Excel file. These coordinates, also called as the "layout coordinates", are used for mapping the motor coordinates of the rest of the devices. Using the Excel file, the system GUI matches the layout coordinates of the grating couplers of the first and last devices to

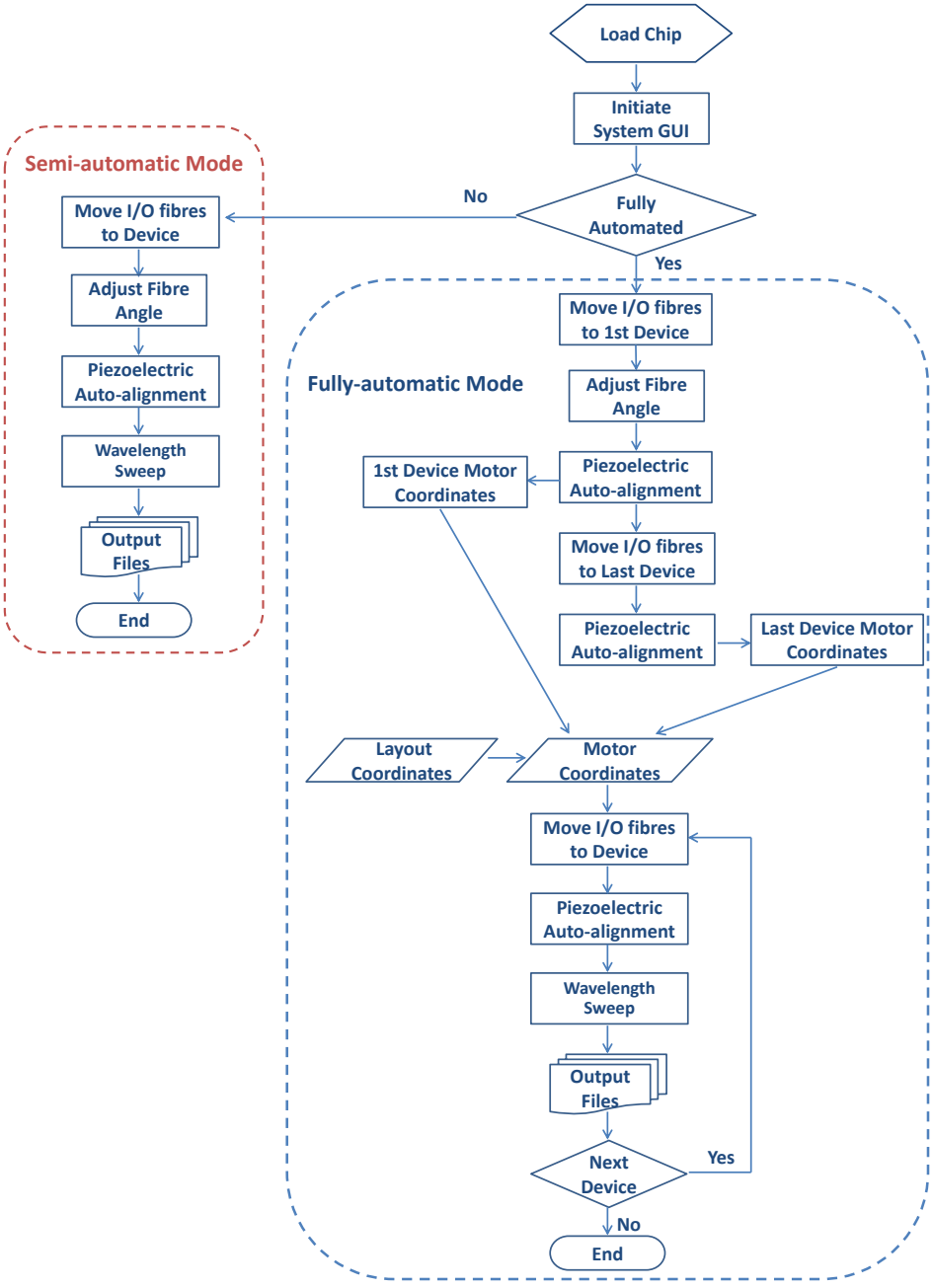

Figure 3.5: Automated Measurement Flowchart.

their motor coordinates, and then calculates the relative chip rotation angles along with the "magnitude scaling constants", which are the ratios of the moving distances calculated from the layout coordinates to those calculated from the motor coordinates of each axis, and thus extrapolates the motor coordinates of rest of the devices based on the assumption that the system errors of the stage movements along each axis have uniform distributions. Hence, the travel paths of the fibres are mapped for auto-alignment. The system GUI then controls the stages to move the fibres, according to the motor coordinates, from one device to another. After moving the fibres to a device, the piezoelectric auto-alignment function is performed to optimize the coupling efficiency between the fibres and the grating couplers. The system GUI then latches the piezoelectric actuators and locks the stepper motors and performs a wavelength sweep of the optical response of the device. The measurements results are then saved to the computer before the system GUI aligns the fibres to the next device.

The measurements in semi-automatic mode have fewer degrees of automation, but have more flexibility and simpler procedures for characterizing devices with various measurement requirements, as compared to those in fully-automatic mode measurements (see Fig. 3.5). In semi-automatic mode, we are able to adjust the incident angles of the input/output fibres for each device to maximize the coupling efficiency for the intended wavelength range. For example, if the output signal of the device is designed to be maximum at shorter wavelengths, then we increase the incident angles of the input/output fibres so that the output power will be maximized at shorter wavelengths. We are also able to set the wavelength range, reso-

lution, and sweep-speed of the tunable laser source on a device-by-device basis. For example, we usually measure a device with a 10 pm wavelength resolution, at a wavelength sweep-speed of 40 nm/s, over the wavelength range from 1480 nm 1580 nm, for high speed wavelength-swept measurements. We can also measure a device with a 1 pm wavelength resolution, at a wavelength sweep-speed of 5 nm/s, over the same wavelength range, for high resolution wavelength-swept measurements.

3.3 24-Hour Alignment Testing

We performed a 24-hour alignment test to evaluate the system stability and measurement repeatability of the automated setup. A single strip waveguide integrated with two grating couplers was chosen for this test. The fibre chucks, loaded with input/output fibres, were rotated to match the polarization of the grating couplers. The incident angles of the fibres were adjusted to maximize the coupling efficiency. The LDC-501 temperature controller was set to keep the experiment operating at 25°C.

The 24-hour alignment test was performed in fully-automatic mode. At the beginning of each hour, during the test, the system GUI aligned the input/output fibres to the strip waveguide using piezoelectric auto-alignment. After the alignment, the stepper motors and the piezoelectric actuators were locked to keep the fibres from moving. The system GUI then performed ten wavelength-swept measurements, with 5 minute intervals between measurements, and saved the measurement results. The system GUI kept locking the motors and the piezoelectric actuators until the end of the tenth measurement. The system GUI then unlocked the motors and piezoelectric actuators and moved the stages back to their "Home" positions at the end of each hour. The system GUI repeated the above procedures every hour during the 24-hour alignment test.

The wavelength-swept measurements covered the wavelength range from 1480 nm to 1580 nm with the wavelength resolution of 10 pm at the sweep-speed of 20 nm/s. Figure. 3.6a shows the power transmission spectrum of the strip waveguide (obtained from the fifth measurement during Hour 1)

with a boxplot showing the power variation of the ten measurements at λ = 1550 nm. During the 24-hour test, the transmission power, as shown in Fig. 3.6b, drifted between -23.35 dBm and -22.59 dBm at λ = 1550 nm. This suggests that the automated measurement setup had relatively stable performance and could provide repeatable measurement results for long duration experiments.

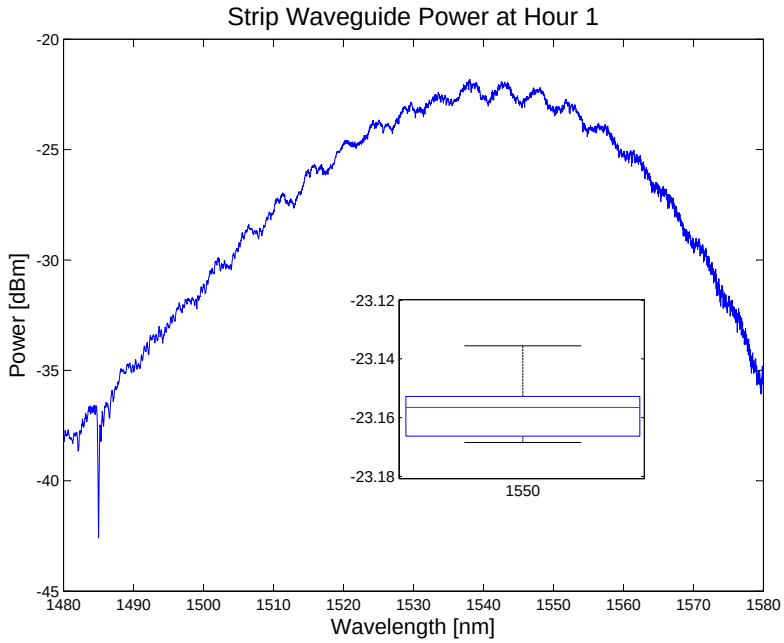

(a)

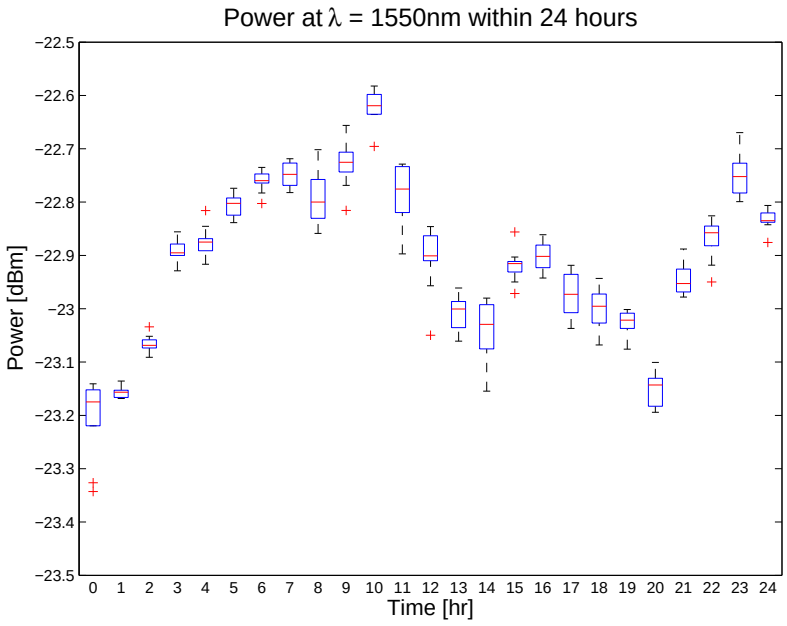

(b)

Figure 3.6: 24-hours alignment test results: (a) Transmission spectrum of a strip waveguide with a boxplot showing the power variation at $\lambda = 1550$nm of ten successive measurements; (b) Power vs. Time at λ= 1550 nm.

Chapter 4

Implementation of Dumbbell Micro-ring Reflector

In this chapter, we present the implementation of a dumbbell shape micro-ring resonator designed for use as a reflective notch filter. The device is designed and analyzed using the transfer-matrix method. We simulated the analytic model of the device and optimized its notch reflection properties. The dumbbell micro-ring reflector was fabricated using the silicon-on-insulator technology and its response measured using the automated optical measurement system. The measurement result showed a reflective response with a quality factor of ∼11,000 and an extinction ratio of 20 dB. We measured and characterized the excess optical loss from the 6-degree Y-branch power splitter that had been integrated into the dumbbell micro-ring reflector. The thermal responses of our device have also been presented.

Sections 4.1 and 4.2 and subsections 4.3.1 and 4.3.2 have been published in Yun et al.[30]. For the convenience of the reader, Sections 4.1 and 4.2 repeat the approach introduced in Chapter 2 for analyzing, modeling, and simulating the dumbbell micro-ring reflector.

4.1 Design and Analysis

4.1.1 Design Scheme

Our device, which contains three directional couplers, has the shape of a dumbbell (see Fig. 4.1a). As shown in Fig. 4.1b, the reflector consists of a dual-coupler micro-ring resonator with an additional directional coupler located at the "handle" of the dumbbell structure to achieve the reflection. The reflected signal consists of the traveling waves from various optical paths within the dumbbell shape structure. For example, for one such path, the input light injected into the port on the left is coupled to a counter-clockwise wave via directional coupler 1. After propagating through waveguide L_2, where L_2 is also the length of waveguide, the light is coupled into a clockwise wave via directional coupler 2 and propagates through the length of waveguide L_4. Thus the light is coupled into a backward traveling wave via directional coupler 3 and becomes a portion of the reflected signal at the left port after passing through directional coupler 1. The reflected traveling wave from the optical path described above is combined with the waves from other reflection paths and resonant paths to form the total reflected signal for the dumbbell micro-ring reflector.

4.1.2 Theoretical Analysis

We use the transfer-matrix method to analyze the reflection properties of the device[27, 28]. We define the field components (labeled in Fig. 4.1b) of

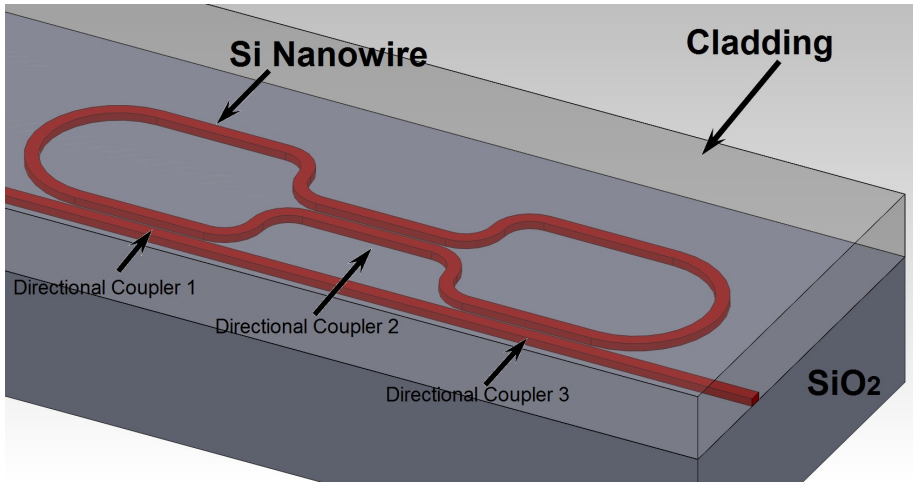

(a)

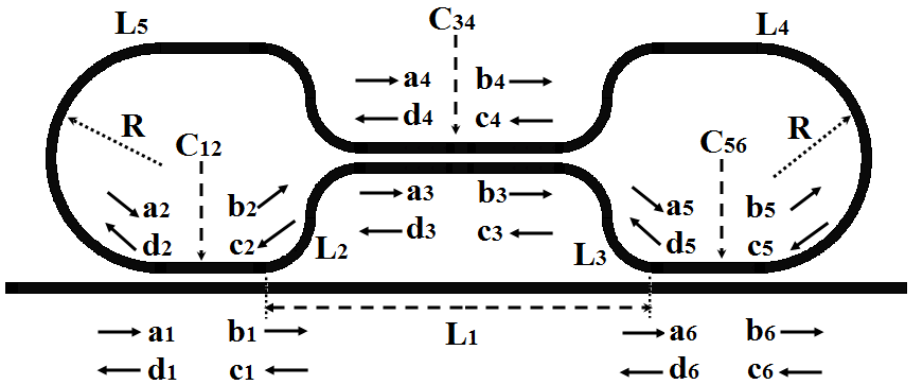

(b)

Figure 4.1: Schematic drawings of dumbbell micro-ring reflector: (a) 3-D schematic on an SOI platform and (b) 2-D schematic with transfer-matrix elements labeled[30]. Copyright 2012 Society of Photo-Optical Instrumentation Engineers.

the directional couplers as:

$$E_i = \begin{bmatrix} a_i & b_i & c_i & d_i \end{bmatrix}^T, \quad i = 1,\ 2,\ 3, ...,\ 6, \tag{4.1}$$

where a_i and b_i represent the field components for the forward traveling waves along the waveguide and c_i and d_i represent the field components for the backward traveling waves.

Assuming that there is no mixing between the forward and backward traveling waves, we can express the coupling relationships for both the forward and backward traveling waves within the directional coupler using a 4×4 coupling matrix[6, 13]:

$$C = \frac{1}{-j\kappa} \begin{bmatrix} -t & 1 & 0 & 0 \\ -t^2 - \kappa^2 & t & 0 & 0 \\ 0 & 0 & -t & 1 \\ 0 & 0 & -t^2 - \kappa^2 & t \end{bmatrix}, \tag{4.2}$$

where $\kappa = |\kappa| e^{-(j\beta + \alpha/2)L_C}$ and $t = |t| e^{-(j\beta + \alpha/2)L_C}$ are the cross-coupling and the straight-through coupling coefficients, respectively, of the directional coupler, β is the propagation constant, α is the propagation loss coefficient, and L_C is the coupling length. Within one directional coupler, the power transmission ratio T_C can be expressed as $T_C = |\kappa|^2 + |t|^2$. We define P_m $(m = 1,\ 2, ...,\ 5)$ as the propagation transfer matrices for light propagating through lengths of waveguides L_m between the directional couplers. With the above expressions and definitions, the relationship between

the left port and the right port of the device is given by

$$E_1 = C_{12}(P_2 C_{34} + P_5)(P_3 C_{34} + P_4)^{-1} C_{56} E_6. \tag{4.3}$$

C_{12}, C_{34}, and C_{56} (see Fig. 4.1b) are the coupling matrices, respectively, between the fields E_i and E_{i+1} ($i = 1,\ 3,$ and 5) within the directional couplers. The propagation matrix in Eq. (4.3), for each waveguide that bridges the directional couplers, is given by

$$P_2 = \begin{bmatrix} 0 & 0 & 0 & 0 \\ P_{L_2}^{-1} & 0 & 0 & 0 \\ 0 & 0 & 0 & P_{L_2} \\ 0 & 0 & 0 & 0 \end{bmatrix} \quad P_3 = \begin{bmatrix} 0 & P_{L_3} & 0 & 0 \\ 0 & 0 & 0 & 0 \\ 0 & 0 & P_{L_3}^{-1} & 0 \\ 0 & 0 & 0 & 0 \end{bmatrix}$$

$$P_4 = \begin{bmatrix} 0 & 0 & 0 & 0 \\ 0 & 0 & P_{L_4}^{-1} & 0 \\ 0 & P_{L_4} & 0 & 0 \\ 0 & 0 & 0 & 0 \end{bmatrix} \quad P_5 = \begin{bmatrix} 0 & 0 & 0 & P_{L_5} \\ 0 & 0 & 0 & 0 \\ 0 & 0 & 0 & 0 \\ P_{L_5}^{-1} & 0 & 0 & 0 \end{bmatrix} \tag{4.4}$$

where $P_{L_m} = e^{-(j\beta + \alpha/2)L_m}$. Assuming that the light is injected only into the left port, i.e., the input signal $a_1 = E_{in}$ and $c_6 = 0$, we can calculate the reflected signal, $E_r = d_1$, by solving Eq. (4.3) with the following additional relationships, which take into account the effect of connecting the two bottom couplers via waveguide L_1:

$$a_6 = P_{L_1} b_1 \text{ and } d_6 = P_{L_1}^{-1} c_1. \tag{4.5}$$

4.2 Simulation and Optimization

4.2.1 Parameters

We designed the dumbbell shape micro-ring reflector based on 500-nm-wide, 220-nm-high, SOI nano-wires (see Fig. 4.2a). The gap distance in all of the directional couplers was 200 nm. We calculated the effective refractive indices using 2-D simulation method[8, 19] (see Fig. 4.2b). The power behavior within a directional coupler can be expressed as a function of the structure of the coupler, the position in the coupler, the coupling coefficient, and the power transmission ratio[14]. In this case, given the coupling gap distance, G, the coupling coefficient, and the power transmission ratio, T_C, we can calculate the coupling length, L_C, of the directional coupler from the following equation:

$$L_C = \arcsin(\frac{|\kappa|}{\sqrt{T_C}}) \cdot (B \cdot e^{-A \cdot G})^{-1}, \tag{4.6}$$

where $A = 9.0842834 \cdot 10^{-3}\ nm^{-1}$ and $B = 1.8670660 \cdot 10^{-4}\ nm^{-1}$ were obtained using Ref. 14.

To take the real situation into account, we also include waveguide propagation loss and coupling loss in our transfer-matrix equation. We use a waveguide propagation loss $\alpha = 5$ dB/cm and a power transmission ratio $T_C = 0.9$, extracted from measurement and experiment data [5, 14] , in our simulations.

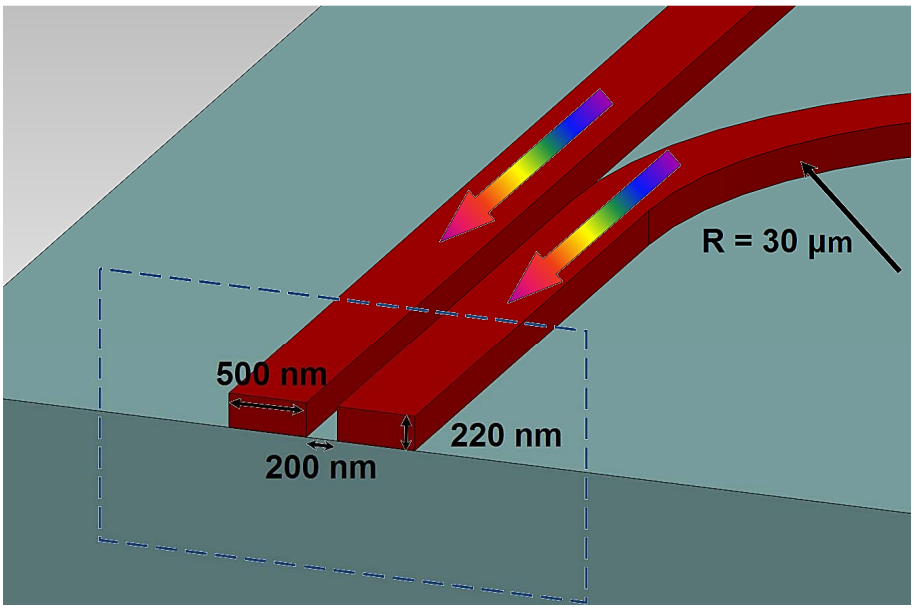

(a)

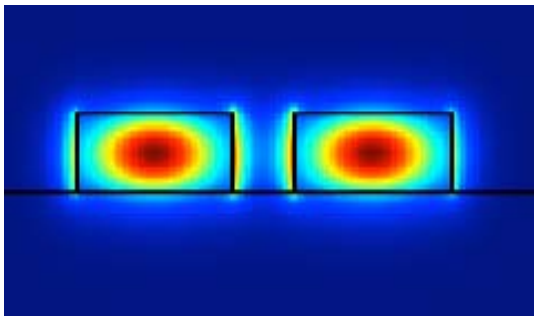

(b)

Figure 4.2: (a) Trimetric view of a directional coupler, with the dimensions labeled ; (b) Mode distribution profile of the symmetric mode in two coupled waveguides[30]. Copyright 2012 Society of Photo-Optical Instrumentation Engineers.

4.2.2 Optimization

The cross-coupling coefficients, κ_{12}, κ_{34}, and κ_{56}, are key factors in determining the performance of the dumbbell micro-ring resonator reflector and, as shown in Fig. 2.9, can significantly affect the magnitude of the reflectivity spectrum as well as the values of the free spectral range and the quality factor. In this case, we defined R_p to be the maximum reflectivity and R_v to be the minimum reflectivity for the various possible combinations of the cross-coupling coefficients of the three couplers. We scanned the reflection spectrum and calculated the reflectivity difference, $R_p - R_v$, and the reflectivity extinction ratio, $10\log_{10}(R_p/R_v)$, as functions of the three cross-coupling coefficients.

The simulation plots in Fig. 4.3 show reflectivity differences and reflectivity extinction ratio values as functions of $|\kappa_{12}|$ and $|\kappa_{56}|$ for a fixed value of $|\kappa_{34}|$. Based on our simulation results, we chose the values for the three cross-coupling coefficients, which were $|\kappa_{12}| = 0.84$, $|\kappa_{34}| = 0.94$, and $|\kappa_{56}| = 0.77$, to meet the requirements of high reflectivity and high extinction ratio.

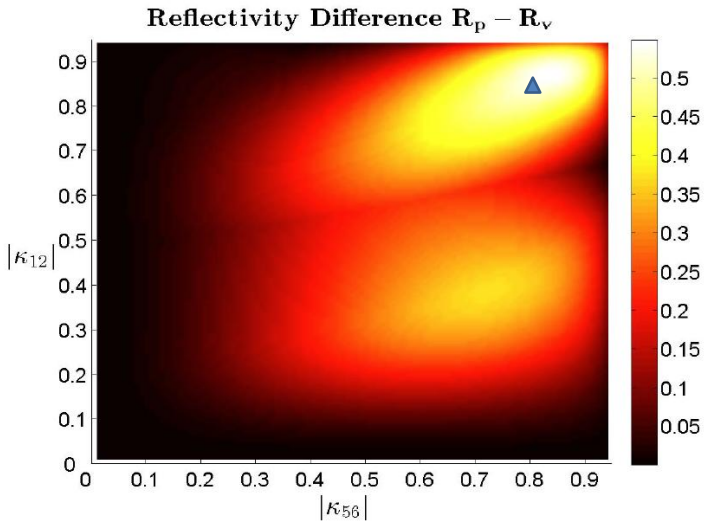

(a)

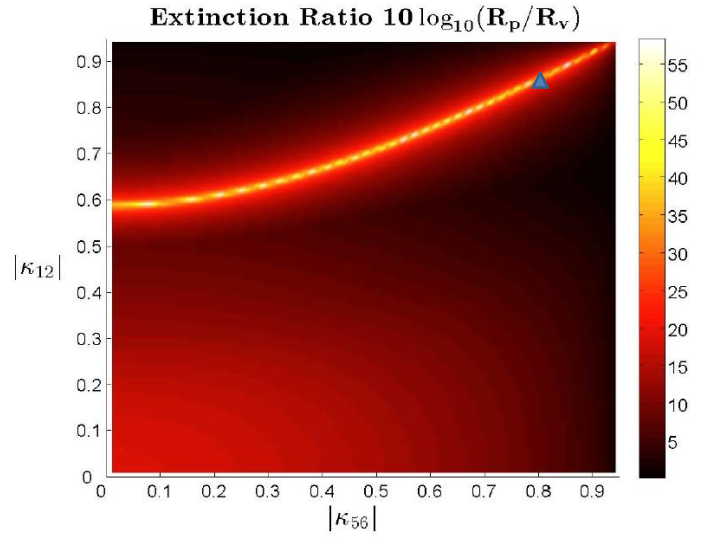

(b)

Figure 4.3: Reflectivity scanning as functions of $|\kappa_{12}|$ and $|\kappa_{56}|$ when $|\kappa_{34}| = 0.94$: (a) Reflectivity differences; (b) Reflectivity extinction ratio[30]. Copyright 2012 Society of Photo-Optical Instrumentation Engineers.

4.3 Fabrication and Characterization

4.3.1 Fabrication

We drew the mask layout using the DW-2000 physical layout and verification software from Design Workshop Technologies[7], and generated the mask layout GDSII file, after passing the DRC (Design Rule Checking), for fabrication. The devices were fabricated at ePIXfab by Imec in Belgium using 193 nm deep UV lithography on SOI platform. Figure. 4.4 shows the fabricated dumbbell micro-ring reflector which has bending radii of 30 μm at the "heads" of the dumbbell, 15 μm in all other bends, and coupler gap distances of 200 nm in the three directional couplers. The coupling lengths of the directional couplers, which are respectively 35.83 μm, 47.30 μm, and 31.20 μm, are also labeled in Fig. 4.4b.

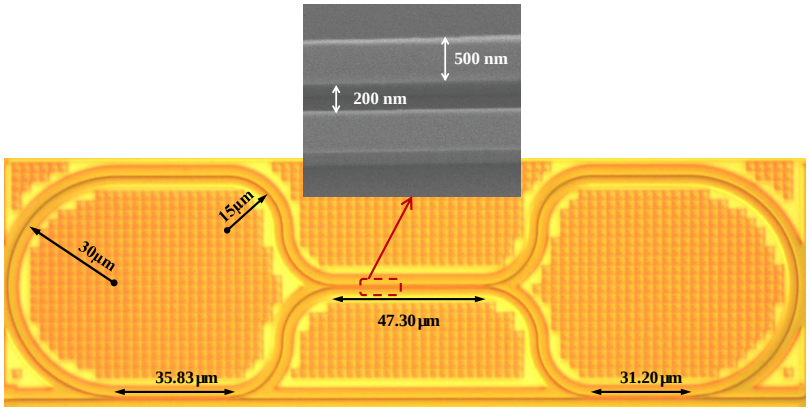

Figure 4.4: Optical image of fabricated dumbbell micro-ring reflector with dimensions labeled and with inset SEM image of the directional coupler.

4.3.2 Reflection Spectra

The schematic for measuring the dumbbell micro-ring reflector using the automated probe station is shown in Fig. 4.5. We used TE-mode periodic grating couplers to couple the light into and out of our optical circuit. A 6-degree Y-branch power splitter[17] was used and integrated into the circuit to split and isolate the reflected signal from the input light.

A single-mode, polarization-maintaining fibre was used as the input fibre, and a multi-mode fibre was used as the output fibre to collect all of the light coming out of the output grating coupler. The incident angles of the fibres were adjusted to maximize the coupling efficiency at $\lambda_0 = 1550$ nm. The fibre chucks were rotated to align the polarization to match the grating couplers. The chip was placed on top of the copper heat sink with an operating temperature setting of 25°C during the measurements.

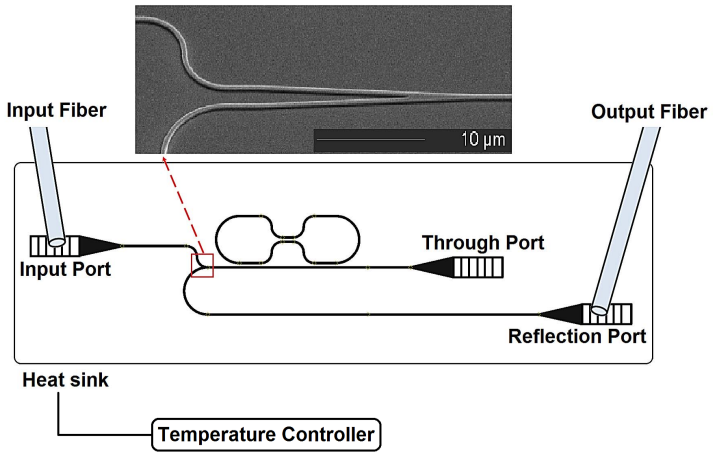

Figure 4.5: Measurement schematic of dumbbell micro-ring reflector with an inset SEM image showing the Y-branch power splitter[30]. Copyright 2012 Society of Photo-Optical Instrumentation Engineers.

Measurements were taken on the reflection port of the device with incident angles of 12° on the input/output fibres (see Fig. 4.6). The reflected power response measured at the reflection port, after calibrating out the loss introduced by the straight waveguide and the two grating couplers between the input port and the reflection port, gave an extinction ratio of 20 dB, a free spectrum range (FSR) of 0.889 nm, and a quality factor (Q) of ∼11,000, which was calculated using

$$Q_{\lambda/\Delta\lambda} = \frac{f_r}{\triangle f} \approx \frac{\lambda_r}{\triangle \lambda_{3\mathrm{dB}}} \tag{4.7}$$

where $\triangle\lambda_{3\mathrm{dB}} = 0.14$ nm is the 3dB wavelength bandwidth as shown in Fig. 4.6.

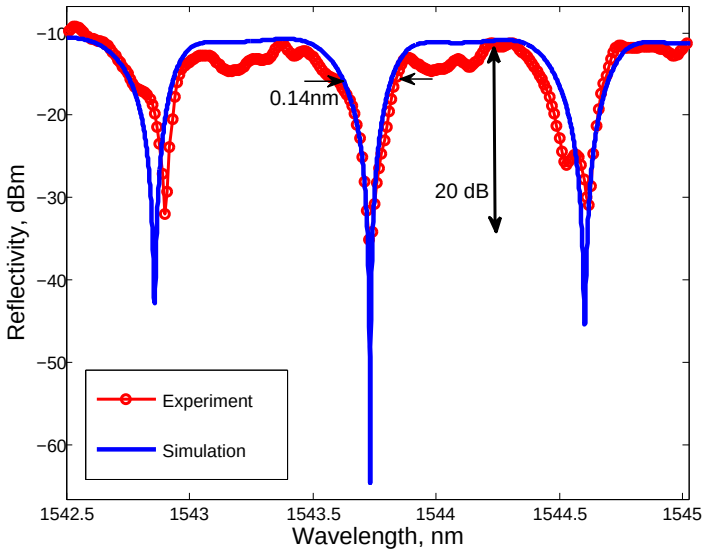

Figure 4.6: Measured and simulated reflection spectra at 25°C (an estimated loss of 7.4 dB from the Y-branch power splitter is included in the simulation data, and the optical paths are tuned to fit the free spectral range and the resonance peaks).

4.3.3 Loss Measurement of Y-branch Splitters Using Micro-ring Resonators

The integrated Y-branch power splitter introduces excess losses to the reflector. Here we used a micro-ring-based method to characterize the optical losses from the integrated Y-branch power splitter, which was independent of the grating coupler insertion losses[16, 18]. The Y-branch power splitter, as shown in Fig. 4.7a, is 20-μm-long with a 6-degree opening angle between its two branch arms and is designed to have a 3 dB optical loss when light travels from its stem waveguide to either of its two branch waveguides.

We designed and fabricated all-pass racetrack micro-ring resonators (not our designed micro-ring reflectors) with several 6-degree Y-branch power splitters integrated inside the ring cavity, as well as a reference micro-ring resonator without any Y-branch splitter (see Fig. 4.7b). Two Y-branch splitters were combined back-to-back to form a symmetric Mach-Zehnder interferometer (MZI) with short arms (6 μm), which avoided the impact of the intrinsic 3 dB loss on the transmission spectrum of the micro-ring. We then inserted various numbers of such MZIs into the ring. The reference micro-ring resonator had a round-trip length of $\sim$544.25 μm with a coupling length of 15 μm and a coupler gap distance of 200 nm. The micro-ring resonators with Y-branch splitters had the same coupler design as the reference micro-ring.

We used the automated setup to measure the transmission spectra of the Y-branch splitter integrated micro-ring resonators, as well as the reference micro-ring resonator. We calculated the coupling coefficient of the 15-μm-

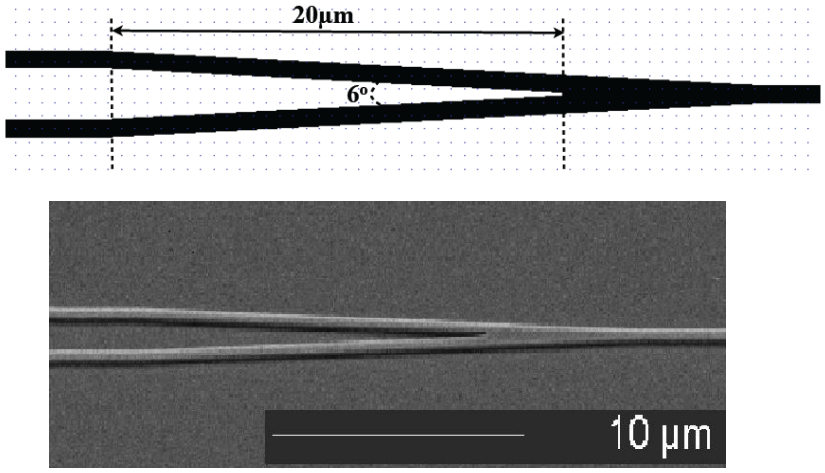

(a)

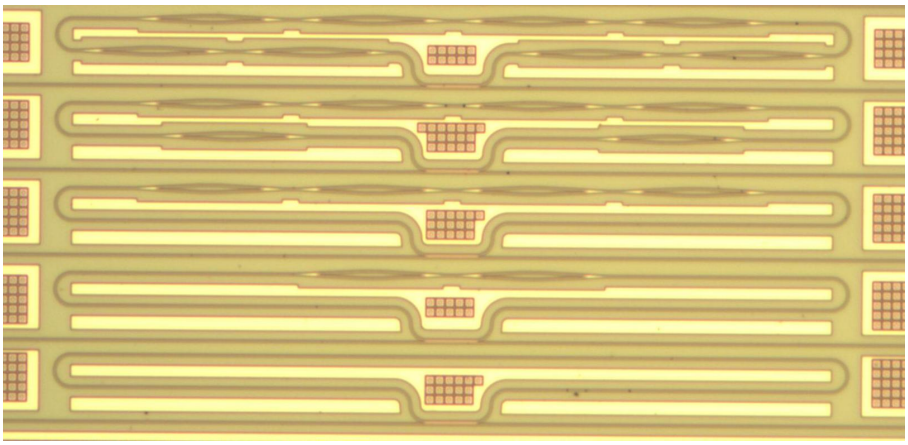

(b)

Figure 4.7: Micro-ring resonators with and without integrated Y-branch splitters: (a) 6-degree Y-branch power splitter mask layout and SEM image; (b) Optical image of fabricated micro-ring resonators with and without Y-branch.

long directional coupler using the 2D FD mode solver. Then we extracted the waveguide loss of the reference micro-ring resonator by curve fitting the measured power transmission spectrum using the following equation[16, 27]:

$$T = \frac{|E_t|^2}{|E_{in}|^2} = \frac{a^2 + t^2 - 2at\cos\delta}{1 + a^2t^2 - 2at\cos\delta} \tag{4.8}$$

where a is the round-trip loss, t is the straight-through coupling coefficient, and δ is the round-trip phase shift. The round-trip phase shift is wavelength dependent and is given by

$$\delta = \frac{2\pi \cdot l \cdot n_{eff}}{\lambda}$$

where l, n_{eff}, and λ are the round-trip length, the effective index, and the wavelength, respectively[27]. Using the same method, we were also able to extract the total round-trip loss of the micro-ring resonator integrated with Y-branch splitters. Thus we could obtain the insertion loss of the Y-branch splitter by subtracting the waveguide loss from the total round-trip loss.

The measured and fit spectra of the reference micro-ring resonator are shown in Fig. 4.8a, for which the round-trip loss is determined to be 0.511 dB. Figure 4.8b shows the measured and fit spectra of the micro-ring resonator with two pairs of Y-branch splitters inserted in the optical cavity, for which the round-trip loss was determined to be 3.322 dB. Table 4.1 lists the values of the parameters that were used for curve-fitting the measured spectra. The excess loss induced by the Y-branch splitters was then extracted and found to be 2.801 dB, which implies an excess loss of $\simeq 0.7$ dB per Y-branch splitter. Thus, the Y-branch power splitter integrated in the

dumbbell micro-ring reflector introduced 7.4 dB optical loss to the reflection response of the reflector, in total. Including this 7.4 dB loss in our simulation, as shown in Fig. 4.6, we fit the simulation results to the measured reflection spectrum.

Device	Reference Micro-ring Resonator	Micro-ring Resonator with two Y-branch pairs
Round-trip Length l [μm]	544.25	547.57
Coupling Coefficient t	0.8982	0.8982
Group Index n_g	4.1989	4.1989
Round-trip Loss α [dB/cm]	9.3963	60.6680

Table 4.1: Parameters for Curve-fitting.

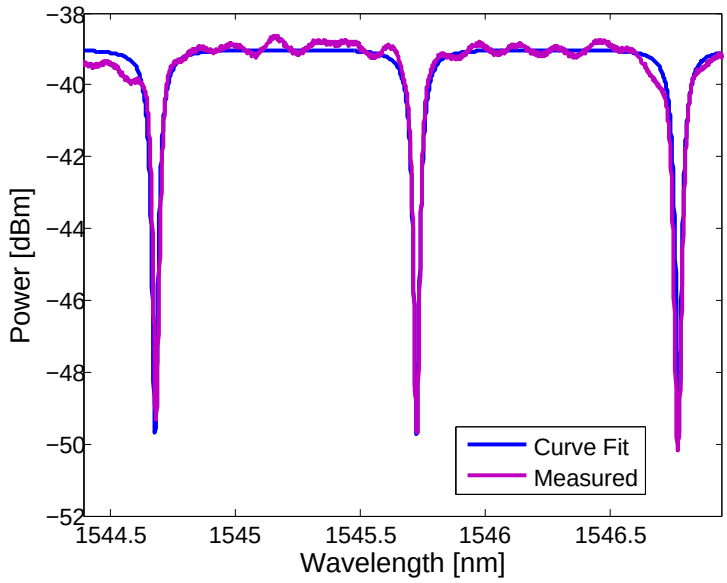

(a)

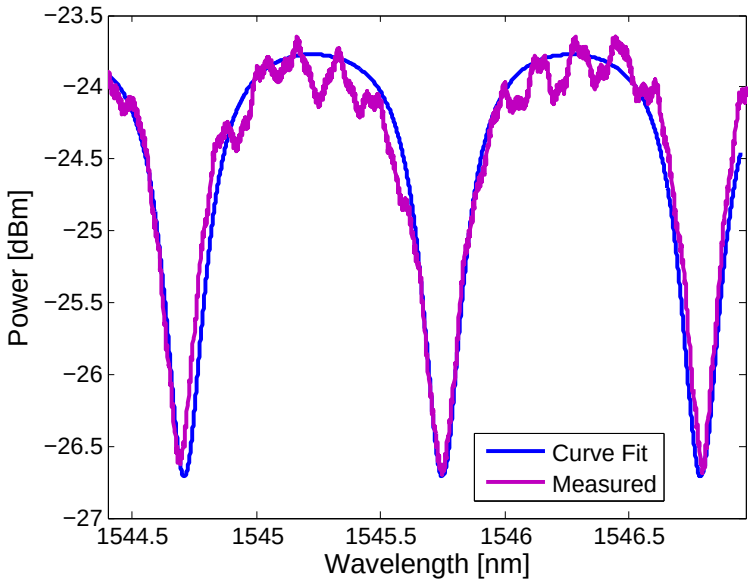

(b)

Figure 4.8: Measured and fit transmission spectra of: (a) a micro-ring resonator; (b) a micro-ring resonator with 2 pairs of Y-branch splitters.

4.3.4 Thermal Tuning Responses

We have also investigated the thermal responses of the dumbbell micro-ring reflector. We controlled the TEC controller to tune the operating temperature. As shown in Fig. 4.9, the resonance peak shifted from ∼1527.50 nm to ∼1528.01nm when the operating temperature was tuned from 22°C to 28°C. To characterize the thermal responses of the device, we tracked the changes of the resonant peak wavelengths by tuning the temperature from 20°C to 40°C in 1°C increment. As shown in Fig. 4.10, curve fitting gives a 0.082 nm/K wavelength shift.

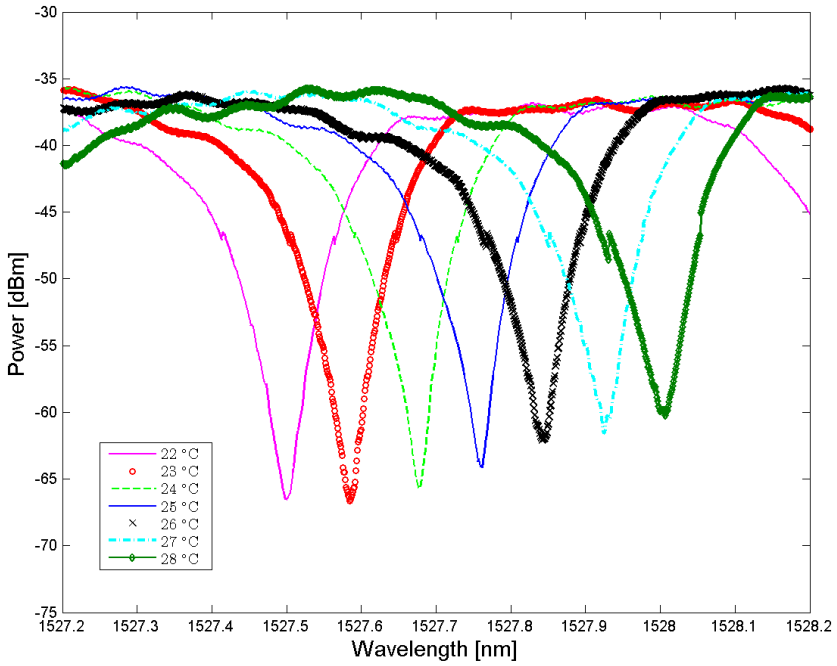

Figure 4.9: Reflection spectra versus temperature tuning at 25±3°C.

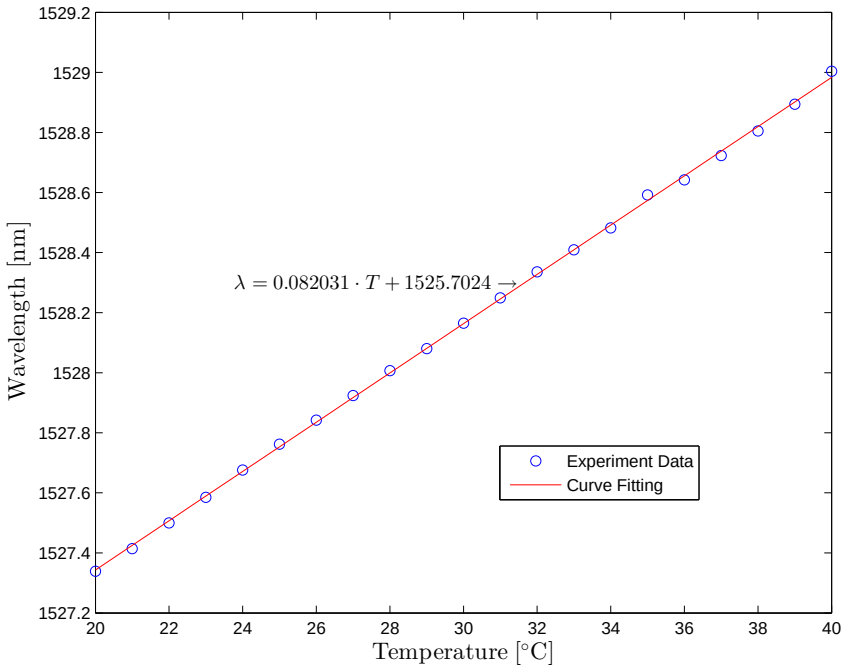

Figure 4.10: Resonant wavelength shift vs. Temperature with curve fitting.

Chapter 5

Summary, Conclusions, and Suggestions for Future Work

5.1 Summary

The design and characterization of an SOI dumbbell micro-ring resonator reflector has been presented in this thesis. Directional couplers were analyzed using the transfer-matrix method, developed from the eigenmode (supermode) theory, to describe the power coupling behavior between the two waveguides and thus to determine the amount of the power that can be coupled from one waveguide to the other. The transfer functions of the add and drop ports of single micro-ring resonator add-drop filters were then derived using the transfer-matrix method, which showed the convenience and simplicity of this matrix formulation. We then applied the transfer-matrix method to obtain the analytic model of the dumbbell micro-ring reflector, and, thus, calculated the reflectivity of the device. We characterized the optical mode of the SOI strip waveguide using a 2-D Finite-Difference eigenmode solver and calculated the coupling lengths of directional couplers using a curve-fit method. We determined the parameters that were used in

the analytic model of the dumbbell micro-ring reflector and optimized our design, base on numerical simulations in MATLAB, for fabrication.

We also designed and assembled a fibre-to-fibre automated optical measurement system. This measurement setup was implemented to automatically characterize on-chip nanophotonic circuits for high speed and high resolution wavelength-swept measurements with accurate fibre alignment. System testing results showed that the setup had relatively stable performance and could provide repeatable measurement results.

We have fabricated an SOI dumbbell micro-ring reflector at ePIXfab by Imec. We measured the reflective responses of the device using the automated measurement setup. Integrated 6-degree Y-branch power splitters were also fabricated and characterized using a micro-ring-based method for calibrating out the optical losses introduced to the dumbbell micro-ring reflector by the Y-branch. The thermal responses of the dumbbell micro-ring reflector were also measured.

5.2 Conclusions

In conclusion, we have demonstrated a wavelength-selective reflector based on a dumbbell shape micro-ring resonator structure. We designed and fabricated the reflector based on silicon nanophotonic waveguides using SOI technology. The measured reflection spectra of the fabricated device showed notch reflective responses. A reflectivity extinction ratio of 20 dB with a Q factor of ∼11,000 and a FSR of 0.889 nm have been achieved when the three directional couplers of the reflector have their respective cross-coupling co-

efficients of 0.84, 0.94, and 0.77. A 0.082 nm/K wavelength shift has also been obtained from the thermal measurement results. Functioning as a reflective notch filter, this reflector geometry can be used for implementing reflective-type electro-optical modulators when carrier injection or depletion mechanisms are incorporated. By monitoring the shift of a resonant wavelength or variation of the reflected light intensity of a fixed wavelength, the dumbbell reflector can be used for either thermal sensing, biochemical sensing, or radio-frequency (RF) electric field detection[20]. Combined with a single optical fiber or integrated with a single strip waveguide for delivering both the input light and reflected signal, the device can be used in remote sensing applications.

5.3 Suggestions for Future Work

The performance of the dumbbell micro-ring reflector, as a notch reflective filter, can be tunned by adjusting the coupling coefficients of the three couplers. Since our simulation optimized the coupling coefficients to two decimal places, higher reflectivity extinction ratios could be achieved by optimizing the coupling coefficients a higher degree. Another approach might be to use the fabrication processes with less waveguide sidewall roughness, and, thus, to improve the device performance by having lower scattering losses. The measured thermal responses also suggest that local thermal heaters can be integrated on the chips to ensure that the device resonates at the designed wavelength.

For the fibre-to-fibre automated measurement setup, following improve-

ments can be made: integrating the functions of the fibre chuck, the holding arm, and the rotation plate into one mechanical part to reduce system errors; using lensed fibres or using manufacture-cleaved fibres to reduce the insertion loss between the fibre and grating coupler; using a two-axis linear long travel motorized stage as the sample stage to increase the measurement range from die-scale to chip-scale, or even to wafer-scale; integrating electric RF/DC probes into the setup for electro-optic measurements.

Bibliography

[1] V. R. Almeida, C. A. Barrios, R. R. Panepucci, and M. Lipson. All-optical control of light on a silicon chip. *Nature*, 431:1081–1084, 2004.

[2] S. Assefa, S. Shank, W. Green, M. Khater, E. Kiewra, C. Reinholm, S. Kamlapurkar, A. Rylyakov, C. Schow, F. Horst, H. Pan, T. Topuria, P. Rice, D. M. Gill, J. Rosenberg, T. Barwicz, M. Yang, J. Proesel, J. Hofrichter, B. Offrein, W. Haensch X. Gu, J. Ellis-Monaghan, and Y. Vlasov. A 90nm CMOS Integrated Nano-Photonics Technology for 25Gbps WDM Optical Communications Applications. *IEEE International Electron Devices Meeting (IEDM), postdeadline session 33.8*, 2012.

[3] W. Bogaerts. Nanophotonic Waveguides and Photonic Crystals in Silicon-on-Insulator. *PhD Thesis*, page 363, 2004.

[4] I. Chremmos and N. Uzunoglu. Reflective Properties of Double-Ring Resonator System Coupled to a Waveguide. *IEEE Photonics Technol. Lett.*, 17:2110–2112, 2005.

[5] L. Chrostowski, N. Rouger, D. Deptuck, and N. A. F. Jaeger. Silicon Nanophotonics Fabrication: an Innovative Graduate Course. *17th*

International Conference on Telecommunications - Optical Communications and Devices, Doha, Qatar, (invited), 2010.

[6] Y. Chung, D-G Kim, and N. Dagli. Reflection Properties of Coupled-Ring Reflectors. *J. Lightwave Technol.*, 24:1865–1874, 2006.

[7] DW-2000. http://www.designw.com/eda-overview.php. Design Workshop and Technologies.

[8] A. B. Fallahkhair, K. S. Li, and T. E. Murphy. Vector Finite Difference Modesolver for Anisotropic Dielectric Waveguides. *J. Lightwave Technol.*, 26:1423–1431, 2008.

[9] B. Jalali and S. Fathpour. Silicon Photonics. *J. Lightwave Technol.*, 24:4600–4615, 2006.

[10] I. P. Kaminow, T. Li, and A. E. Willner. *Optical Fiber Telecommunications V A (Fifth Edition): Components and Subsystems.* Academic Press, 2008.

[11] C. Lin. Photonic device design flow : from mask layout to device measurement. *Thesis*, page 97, 2012.

[12] J. D. Meindl. Beyond Moore's law: the interconnect era. *Computing in Science and Engineering*, 5:20–24, 2003.

[13] J. K. S. Poon, J. Scheuer, and A. Yariv. Wavelength-Selective Reflector Based on a Circular Array of Coupled Microring Resonators. *IEEE Photonics Technol. Lett.*, 16:1331–1333, 2004.

[14] N. Rouger, L. Chrostowski, and R. Vafaei. Temperature Effects on Silicon-on-Insulator (SOI) Racetrack Resonators: A Coupled Analytic and 2D Finite Difference Approach. *J. Lightwave Technol.*, 28:1380–1392, 2010.

[15] W. Shi. Silicon Photonic Filters for Wavelength-Division Multiplexing and Sensing Applications. *Thesis*, page 121, 2012.

[16] W. Shi, T. K. Chang, H. Yun, W. Zhang, C. Lin, Y. Wang, N. A. F. Jaeger, and L. Chrostowski. Differential Measurement of Transmission Losses of Integrated Optical Components Using Waveguide Ring Resonators. *Proc. SPIE, Photonics North 2012*, 8412:84120R, 2012.

[17] W. Shi, R. Vafaei, M. A. Torres, N. A. F. Jaeger, and L. Chrostowski. Design and characterization of microring reflectors with a waveguide crossing. *Opt. Lett.*, 35:2901–2903, 2010.

[18] W. Shi, H. Yun, W. Zhang, C. Lin, T. K. Chang, Y. Wang, N. A. F. Jaeger, and L. Chrostowski. Ultra-compact, high-Q silicon microdisk reflectors. *Opt. Express*, 20:21840–21846, 2012.

[19] MODE Solutions. http://www.lumerical.com/tcad-products/mode/. Lumerical Solutions, Inc.

[20] H. Sun, A. Chen, and L. R. Dalton. A reflective microring notch filter and sensor. *Opt. Express*, 17:10731–10737, 2009.

[21] Agilent Technologies. 81480A and 81680/640/682/689A Tunable Laser Modules Users Guide. 2001.

[22] Agilent Technologies. 81630B/4B/6B/7B Power Sensor Modules and 81635A Dual Power Sensor Module User's Guide. 2002.

[23] Agilent Technologies. 8163A/B, 8164A/B, and 8166A/B User's Guide. 2004.

[24] Inc. Thorlabs. APT Modular Rack: Model Number MMR601 MMR602. 2008.

[25] Inc. Thorlabs. HFC005 and HFC007 Fibre Chucks - Manual. 2011.

[26] Inc. Thorlabs. MAX300 Series NanoMax 3-Axis Flexure Stage User Guide. 2012.

[27] A. Yariv and P. Yeh. *Photonics: Optical Electronics in Modern Communications*. Oxford University Press, New York, 2007 (sixth edition).

[28] Amnon Yariv. Coupled-Mode Theory for Guided-Wave Optics. *IEEE J. Quantum Electron.*, QE-9:919–933, 1973.

[29] H. Yun, W. Shi, X. Wang, L. Chrostowski, and Nicolas A. F. Jaeger. Design of a Microring Reflector with a Dumbbell Structure. *The 15th Canadian Semiconductor Science and Technology Conference*, 2011.

[30] H. Yun, W. Shi, X. Wang, L. Chrostowski, and Nicolas A. F. Jaeger. Dumbbell Micro-Ring Reflector. *Proc. SPIE, Photonics North 2012*, 8412:84120P, 2012.